Predictions for low-p_T and high-p_T hadron spectra in nearly central Pb+Pb collisions at $\sqrt{s_{NN}} = 5.5$ TeV tested at $\sqrt{s_{NN}} = 130$ and 200 GeV

K. J. Eskola,[1,2,*] H. Honkanen,[1,2,3,†] H. Niemi,[1,2,‡] P. V. Ruuskanen,[1,2,‖] and S. S. Räsänen[1,¶]

[1]*Department of Physics, P.B. 35, FIN-40014 University of Jyväskylä, Finland*

[2]*Helsinki Institute of Physics, P.B. 64, FIN-00014 University of Helsinki, Finland*

[3]*Department of Physics, University of Virginia, P.O.B. 400714, Charlottesville, Virginia 22904-4714, USA*

(Received 9 June 2005; published 31 October 2005)

We study the hadron spectra in nearly central $A+A$ collisions at the Relativistic Heavy Ion Collider (RHIC) and the Large Hadron Collider (LHC) in a broad transverse momentum range. We cover the low-p_T spectra using longitudinally boost-invariant hydrodynamics with initial energy and net-baryon number densities from the perturbative QCD (pQCD)+saturation model. Buildup of the transverse flow and sensitivity of the spectra to a single decoupling temperature $T_{\rm dec}$ are studied. Comparison with RHIC data at $\sqrt{s_{NN}} = 130$ and 200 GeV suggests a rather high value $T_{\rm dec} = 150$ MeV. The high-p_T spectra are computed using factorized pQCD cross sections, nuclear parton distributions, fragmentation functions, and describing partonic energy loss in the quark-gluon plasma by quenching weights. Overall normalization is fixed on the basis of $p+\bar{p}(p)$ data and the strength of energy loss is determined from RHIC Au+Au data. Uncertainties are discussed. With constraints from RHIC data, we predict the p_T spectra of hadrons in 5% most central Pb+Pb collisions at the LHC energy $\sqrt{s_{NN}} = 5500$ GeV. Because of the closed framework for primary production, we can also predict the net-baryon number at midrapidity, as well as the strength of partonic energy losses at the LHC. Both at the LHC and RHIC, we recognize a rather narrow crossover region in the p_T spectra, where the hydrodynamic and pQCD fragmentation components become of equal size. We argue that in this crossover region the two contributions are to a good approximation mutually independent. In particular, our results suggest a wider p_T region of applicability for hydrodynamical models at the LHC than at RHIC.

DOI: 10.1103/PhysRevC.72.044904 PACS number(s): 24.85.+p, 25.75.Nq, 12.38.Bx, 24.10.NZ

I. INTRODUCTION

Transverse-momentum spectra of hadrons in ultrarelativistic heavy-ion collisions offer invaluable input for the studies of quantum chromodynamics (QCD) matter properties and QCD dynamics. At high collision energies, currently at the Brookhaven National Laboratory Relativistic Heavy Ion Collider (RHIC) and in the near future at the CERN Large Hadron Collider (LHC) the parton and hadron production rates are significant over a wide transverse momentum range. The high- and low-p_T parts of the transverse-momentum spectra provide complementary information on the QCD matter. As reviewed below, the hadron spectra measured in Au+Au collisions at RHIC show systematic evidence on formation of elementary-particle matter and provide motivation for hydrodynamical description of $A+A$ collisions.

A. Large energy densities

First, average initial energy densities can be estimated on the basis of measured transverse energy [1] originating from the low-p_T region of the hadron spectra. Even the conservative Bjorken estimate [2], $\epsilon = dE_T/d\eta/(\pi R_A^2 \tau)$, computed using $dE_T/d\eta = 606 \ldots 620$ GeV as measured at $\eta \sim 0$ in $0 \ldots 5\%$ central Au+Au collisions at $\sqrt{s_{NN}} = 200$ GeV at RHIC, implies an average local energy density $\epsilon \approx 5$ GeV/fm^3 [1] at $\tau \sim 1$ fm, a typical hadronization time in a $p+p$ collision in vacuum. Already this is well above the energy densities where hadrons could form. Because the formation time of such a system at RHIC is most likely considerably shorter than 1 fm, the average initial energy densities can be expected to be clearly, say, even a factor of 5, higher. Furthermore, if there is pressure in the system, the estimates of energy density become even larger, because dE_T/dy is not conserved due to the pdV work by pressure in longitudinal expansion. According to the hydrodynamic studies, the initial-to-final transverse energy degradation can be as much as a factor of 3 [3], increasing the initial energy density estimates accordingly.

B. Pressure

Second, clear azimuthal asymmetry in the transverse spectra has been observed [4] in noncentral collisions. This phenomenon is possible only if sufficiently frequent secondary collisions take place to build up pressure. Furthermore, hydrodynamic studies imply that the pressure must form early enough (in less than 1 fm) for the spatial azimuthal asymmetry in the primary production to be transferred into momentum distributions [5]. Complete thermalization, however, is not necessary for generating pressure in the system. Both observations, the large energy densities and the early existence of pressure, considered together suggest that a collectively behaving partonic matter of gluons, quarks, and antiquarks, is produced.

*E-mail address: kari.eskola@phys.jyu.fi
†E-mail address: heli.honkanen@phys.jyu.fi
‡E-mail address: harri.niemi@phys.jyu.fi
‖E-mail address: vesa.ruuskanen@phys.jyu.fi
¶E-mail address: sami.rasanen@phys.jyu.fi

C. Partonic energy loss

Third, the high-p_T hadron spectra in Au+Au collisions at $p_T \gtrsim 4 \cdots 5$ GeV have been observed to be suppressed by a factor $\sim 4 \cdots 5$ relative to $p+p$ [6–11]. This energy loss, jet quenching, is one of the predicted quark-gluon plasma (QGP) signals [12]. The fact that no such suppression is discovered in d+Au collisions [13] excludes the possibility that the primary QCD collision mechanism for producing high-p_T partons in nuclear collisions would be very different from that in $p+p$. Also the back-to-back correlation of the high-p_T hadrons, present in the $p+p$ collisions, has been observed to disappear in central Au+Au [14]. These results, considered together with the first two, very strongly suggest that the origin of the observed high-p_T suppressions in Au+Au is the produced partonic medium: before hadronization the hard partons lose energy in penetrating through the dense parton matter.

D. Hydro for low-p_T and pQCD for high-p_T spectra

The interpretation of the HBT radii extracted from the particle correlation measurements [15] is still a puzzle to be solved for a better understanding of the produced collective system. Despite this caveat, the RHIC results discussed in the previous paragraphs indicate that a dense strongly interacting partonic system, where mean free paths are much smaller than the size of the system, is produced in nonperipheral $A+A$ collisions. It is then reasonable to expect that hadron spectra at $p_T \lesssim 2 \ldots 3$ GeV, the region that dominates the total multiplicity and transverse energy, can be obtained by treating the expansion of produced matter quantitatively in terms of relativistic hydrodynamics [16]. Several pieces of input are necessary for such calculation: initial state of the evolution must be given in detail, an equation of state (EOS) is needed to close the system of hydrodynamic equations and finally the collective description of flowing matter must be turned into particle spectra.

In the hydrodynamic approach also the originally produced high-p_T partons are assumed to be absorbed into the thermalized system and all final-state hadrons are thermally emitted from the decoupling surface. Especially, no remnants of pQCD power-law tails are left on top of the steeply falling thermal spectra of hadrons. In the spectra of hadrons measured in Au+Au collisions at RHIC, the powerlaw-like tails do appear at large transverse momenta, $p_T \gtrsim 5.6$ GeV, but because the high-p_T partons carry only a small fraction of the total (transverse) energy, the assumption that all partons thermalize does not affect the treatment of the thermal part appreciably. For the high-p_T region, a more relevant baseline calculation is hadron production without rescatterings, where all the produced high-p_T partons cascade in vacuum into noninteracting partonic showers that then independently hadronize. Such reference spectra can be computed for $A+A$ collisions using perturbative QCD (pQCD) in the same way as in $p+\bar{p}$ and $p+p$ collisions. Energy losses can also be incorporated into these baseline spectra [12].

E. In this paper

We aim to comprehensively describe hadron spectra in central $A+A$ collisions, comparing the results with RHIC data and giving detailed predictions for the 5% most central Pb+Pb collisions at the LHC. On one hand, we compute the spectra within the framework of hydrodynamics, applying initial conditions predicted by pQCD and saturation [3,17] and also including decays of produced resonances after decoupling. On the other hand, we compute the high-p_T reference spectra in the framework of collinearly factorized pQCD cross sections, nuclear parton distributions (nPDFs), and fragmentation functions [18]. Following Ref. [19], energy losses of high-p_T partons are incorporated in terms of quenching weights [20]. A comparison of the computed low- and high-p_T spectra with RHIC data is presented and, in particular, these spectra are predicted for the 5% most central Pb+Pb collisions at the LHC. We also determine and discuss the theoretically challenging crossover region where the hydrodynamic and the pQCD spectra are comparable. For RHIC energies, other studies combining hydrodynamics with a saturation-inspired initial state and jet quenching can be found in Ref. [21], and a discussion on the crossover region in Ref. [22].

The rest of this article is arranged as follows: In Sec. II, we first briefly review the saturation models from which the initial state for hydrodynamics can be computed at collider energies. After this, we discuss in more detail the pQCD+saturation initial conditions. In Sec. III we define the hydrodynamic framework. In particular, we discuss the fast thermalization assumption, the EOS, and collective flow phenomena. Section IV specifies the pQCD computation of the baseline high-p_T spectra without and with energy losses. The results are presented in Sec. V, and conclusions in Sec. VI.

II. INITIAL STATE FOR HYDRODYNAMICS

A key input for hydrodynamical studies is the initial state of evolution. At the SPS energies, hadron multiplicities and spectra have been used to constrain the initial state, the EOS, flow and decoupling [23,24]. However, it turned out that different combinations of initial states and EOS can lead to similar results for the final spectra. Hence, the spectra could obviously be more efficiently used to extract information on the properties of QCD matter and its spacetime evolution if the initial state could be extracted from elsewhere. This can be expected to be the case at collider energies as perturbatively computable parton production may dominate initial parton production in $A+A$ collisions at sufficiently high collider energies [25–28]. Because of the diverging partonic cross sections, pQCD alone, however, does not predict the amount of transverse energy deposited into the central rapidity region. A further element, such as gluon saturation, is needed. We briefly comment on the saturation models that provide a basis for estimating the initial conditions.

A. A brief review of saturation models

1. The general idea in saturation—evidence in DIS

Gluon saturation was introduced more than two decades ago for $p+p$ collisions [29] as a property of the wave functions of the incoming hadrons that makes the primary gluon production finite and preserves unitarity. At sufficiently small momentum fractions x and small scales Q^2, the evolution dynamics of

gluon distributions (BFKL [30] or DGLAP [31]) is expected to become dominated by gluon fusions rather than splittings, inhibiting the growth of the gluon distributions toward smaller x or higher Q^2 and leading to saturation. The idea has been successfully tested in the case of the free proton: geometric scaling of the structure function F_2^p at small x and small Q^2 predicted by the dipole picture [32] has been observed. Also the leading-order (LO) DGLAP fits to the HERA data in the region $x \sim 10^{-5}$, and $Q^2 \sim 1.5\,\mathrm{GeV}^2$ improves after including nonlinearities [29,33] induced by the gluon fusions [34]. Extrapolation to nuclei, however, is more model dependent, see, e.g., Refs. [35,36].

2. Saturation in A+A—semianalytical models

In the context of ultrarelativistic heavy-ion collisions, the idea of gluon saturation in the wave functions of the colliding nuclei governing and regulating the final-state particle production was discussed first in Ref. [25]. It was suggested that particle production in high energy $A+A$ collisions could be computed in perturbative QCD (pQCD) as the saturation scale $Q_{\mathrm{sat}} \propto A^{1/6}$ becomes large, $Q_{\mathrm{sat}} \gg \Lambda_{\mathrm{QCD}}$. More recently, initial gluon production in $A+A$ collisions was computed semianalytically in Refs. [37,38] by applying k_T factorization to $2 \to 1$ processes. In this approach, the shape of final state rapidity distributions is taken to be directly that of initially produced gluons, and the overall normalization is fixed on the basis of RHIC data at one energy. Good fits to the multiplicities and pseudorapidity distributions at RHIC have been obtained [37] and predictions for the LHC have been made [38]. It is, however, useful to recall the theoretical uncertainties of this approach. Widening of the rapidity distributions due to secondary collisions, as demonstrated by longitudinally boost-noninvariant hydrodynamics [24,39,40], is neglected. This phenomenon affects off-central rapidities more than the central ones. There are also uncertainties in the determination of the saturation region for nuclei (see also Ref. [35]) as well as in the specific form of the unintegrated nuclear gluon distributions in the saturation region and also at large x (see the discussion in Ref. [41]). Detailed hydrodynamic studies where the initial state is based on k_T-factorized gluon production at RHIC energies, can be found in Ref. [21].

3. Color glass condensate model for A+A—a lattice approach

The idea of saturation in ultrarelativistic heavy-ion collisions was exploited also in the color-glass condensate (CGC) model [42], where the small-x gluons are described by classical gauge fields. Over the recent years this model has experienced a very active stage of development; for recent reviews see, e.g., Ref. [43]. With boost-invariance the CGC model becomes an effective three-dimensional theory. Primary gluon production can then be computed nonperturbatively by assuming a Gaussian distribution of random color charges and solving the classical Yang-Mills equations on a lattice. For the SU(3) case, this was first done in Ref. [44]. The too large transverse momentum relative to the multiplicity obtained from the calculation was, however, a puzzle (see, e.g. [45]) that was solved only recently in Ref. [46]. The lattice approach, however, does not provide a value for the saturation scale and thus no absolute *prediction* for the initial state, either. As discussed in [44,46], the predicted initial state of matter can range between *(i)* a dilute system of gluons, which only fragment into more gluons but do not interact with each other (as in the scenario of Ref. [37] discussed above), and *(ii)* a very dense system where gluons interact vividly and where the initially produced multiplicity is essentially the final multiplicity but transverse energy is clearly larger than the final E_T. The latter case is equivalent to what is predicted in the pQCD+saturation+hydrodynamics model [3,17] discussed below. The nonperturbative CGC model [46] or the semi-analytical k_T factorization model [37,38] can be used to predict the initial state at the LHC if the saturation scales and unintegrated gluon densities can be extracted and the form of color density fluctuations constrained on the basis of deep inelastic F_2^A data for nuclei [47,48].

4. pQCD+final state saturation model in A+A

In the pQCD+saturation model [17], a dense initial state with large transverse energy is predicted by requiring saturation among the *produced* gluons [17,60] in the same spirit as was originally suggested [25,29] for the initial state. Parton production in a midrapidity unit Δy in a central $A+A$ collision is computed by applying collinearly factorized pQCD cross sections with nuclear parton distributions obtained from a global DGLAP fit [49] to nuclear deep inelastic scattering and Drell-Yan data. The parton production is allowed to continue from large p_T partonic jets, where pQCD is known to work, down to a semihard transverse momentum cutoff $p_0 \gg \Lambda_{\mathrm{QCD}}$. If the production is abundant enough the cutoff p_0 can be defined from saturation as follows: let the number of produced partons (gluons clearly dominate) at $p_T \geqslant p_0$ in a central ($\mathbf{b} = 0$) collision be $N_{AA}(\mathbf{0}, p_0, \Delta y, \sqrt{s})$ and the effective transverse area occupied by each parton to be proportional to π/p_0^2. At saturation the partons fill the whole transverse overlap area πR_A^2, and the effective saturation scale $p_0 = p_{\mathrm{sat}}$ is a solution of a saturation criterion

$$N_{AA}(\mathbf{0}, p_0, \Delta y = 1, \sqrt{s}) \cdot \pi \big/ p_0^2 = \pi R_A^2. \tag{1}$$

We have taken the possible constant of proportionality in front of π/p_0^2, which might contain, e.g., α_s or group theoretical color factors, equal to 1.

Gluons with $p_T \leqslant p_{\mathrm{sat}}$ form at later times, $\tau > 1/p_{\mathrm{sat}}$, and they fuse together with gluons formed earlier. In this sense, the number of produced partons saturates. The number of partons at saturation, $N_{AA}(p_{\mathrm{sat}})$, gives a fair estimate of the total multiplicity of produced partons, provided that $p_{\mathrm{sat}} \gg \Lambda_{\mathrm{QCD}}$. The formation time of the dominant part of the system is then $\tau_0 \sim 1/p_{\mathrm{sat}}$. With the saturation condition of Eq. (1), the computation of the initial state is closed and can be done at any energy. Total transverse energy deposit and initial energy density at τ_0 can be computed including the next-to-leading order contributions in minijet production [50]. Benefits over the other approaches discussed above, are that chemical decomposition and especially the net-baryon number content of the initial state are also obtained [51].

The pQCD+(final state) saturation approach obviously does not suggest a microscopic dynamical mechanism for saturation, although the general idea of produced gluons to act

as a medium for the to-be-produced gluons, is similar to the self-screening suggested in Ref. [52]. The pQCD+saturation model, rather, serves as a useful effective tool in estimating the magnitude of initial parton production in simplest situations where only one scale dominates the production, as in central and nearly central collisions at midrapidities. Despite the possibly large theoretical uncertainties, the pQCD+saturation model, combined with hydrodynamics, i.e., isentropic space-time evolution, correctly *predicted* the multiplicities measured in nearly central Au+Au collisions at RHIC at $\sqrt{S_{NN}} = 56$, 130, and 200 GeV [3,17,53].

Also the low-p_T spectra of pions, kaons, and protons measured in 5% central Au+Au collisions at $\sqrt{S_{NN}} = 130$ GeV at RHIC are simultaneously reproduced surprisingly well [54,55] by pQCD+saturation+hydrodynamics, provided that the hydrodynamic evolution decouples at rather high temperature, $T_{\rm dec} \approx 150$ MeV. Such a high decoupling temperature has also been suggested in a fireball parametrization [56]. Motivated by the success of the pQCD+saturation+hydrodynamics model, we here extend the study of Ref. [54] to $\sqrt{S_{NN}} = 200$ GeV at RHIC and $\sqrt{S_{NN}} = 5500$ GeV at the LHC as well.

B. Initial densities from pQCD+saturation

According to collinear factorization and LO pQCD, the inclusive cross section of two-parton production in $A+B$ collisions is given by the following:

$$\frac{d\sigma^{AB\to kl+X}}{dp_T^2 dy_1 dy_2} = \sum_{ij} x_1 f_{i/A}(x_1, Q^2) x_2 f_{j/B}(x_2, Q^2) \frac{d\hat{\sigma}^{ij\to kl}}{d\hat{t}}(\hat{s}, \hat{t}, \hat{u}), \quad (2)$$

where $f_{i/A}$ and $f_{j/B}$ are the number densities of partons i and j in the beams A and B and $x_{1,2}$ are the fractional momenta of i and j. The hatted symbols are the Mandelstam variables of the partonic $2 \to 2$ subprocesses, with cross section $\hat{\sigma} \propto \alpha_s^2$. The partons k and l are produced back-to-back in transverse plane, with transverse-momentum p_T for each and rapidities y_1 and y_2. We choose the factorization and renormalization scales to be identical and set $Q = p_T$. In certain cases, such as jet production [57] and minijet transverse energy production [50], the computation can be rigorously extended to next-to-leading order (NLO) pQCD. In these cases, a K factor that simulates the NLO contributions can be defined and determined.

Consider now partons only above a minimum scale $p_0 \gg \Lambda_{\rm QCD}$, where the pQCD computation is still reliable. Using Eq. (2), the number (N^f) and transverse energy (E_T^f) distributions for partons of flavor f falling into a rapidity interval Δy can be defined as [27,51]

$$\left.\frac{d\sigma}{dX^f}\right|_{\substack{y_f\in\Delta y \\ p_T \geqslant p_0}} = \int dp_T^2 dy_1 dy_2 \sum_{\langle kl\rangle} \frac{d\sigma^{AB\to kl+X}}{dp_T^2 dy_1 dy_2} \frac{1}{1+\delta_{kl}} \times \delta\Big\{X^f - p_T^{n(X^f)}[\delta_{fk}\theta(y_1 \in \Delta y) + \delta_{fl}\theta(y_2 \in \Delta y)]\Big\}\theta(p_T \geqslant p_0), \quad (3)$$

where the power $n(X^f) = 0$ when $X^f = N^f$, and $n(X^f) = 1$ when $X^f = E_T^f$. The first momenta of these distributions become

$$\sigma\langle X^f\rangle_{\Delta y, p_0} = \int dp_T^2 dy_1 dy_2 \sum_{\substack{ij \\ \langle kl\rangle}} x_1 f_{i/A}(x_1, Q^2) x_2 f_{j/B}(x_2, Q^2) \frac{1}{1+\delta_{kl}} \times \left[\delta_{fk}\frac{d\hat{\sigma}^{ij\to kl}}{d\hat{t}}(\hat{s}, \hat{t}, \hat{u}) + \delta_{fl}\frac{d\hat{\sigma}^{ij\to kl}}{d\hat{t}}(\hat{s}, \hat{u}, \hat{t})\right] \times p_T^{n(X^f)}\theta(y_1 \in \Delta y)\,\theta(p_T \geqslant p_0). \quad (4)$$

For an $A+B$ collision at an impact parameter $\mathbf{b}$, the average number of partons produced with $y \in \Delta y$ and $p_T \geqslant p_0$ can then be obtained as

$$N_{AB}^f(\mathbf{b}, p_0, \Delta y, \sqrt{s}) = T_{AB}(\mathbf{b})\sigma\langle N^f\rangle_{\Delta y, p_0} \quad (5)$$

and their transverse energy as

$$E_{T,AB}^f(\mathbf{b}, p_0, \Delta y, \sqrt{s}) = T_{AB}(\mathbf{b})\sigma\langle E_T^f\rangle_{\Delta y, p_0}. \quad (6)$$

The nuclear overlap function,

$$T_{AB}(\mathbf{b}) = \int d^2\mathbf{r} T_A(\mathbf{b}-\mathbf{r}) T_B(\mathbf{r}), \quad (7)$$

where $\mathbf{r} = (x, y)$, is defined as usual, through the thickness function $T_A(\mathbf{r}) = \int dz \rho_A(z, \mathbf{r})$, where $\rho_A(z, \mathbf{r})$ is the nuclear density. We shall use the spherically symmetric Woods-Saxon nuclear density [58]. Below, the flavor-summed quantities (N and E_T) appear without the index f. The net-baryon number carried into the rapidity acceptance Δy by the $p_T \geqslant p_0$ minijets is then one-third of the produced net quark number [51],

$$N_{AB}^{B-\overline{B}}(\mathbf{b}, p_0, \Delta y, \sqrt{s}) = T_{AB}(\mathbf{b})\frac{1}{3}\sum_q [\sigma\langle N^q\rangle_{\Delta y, p_0} - \sigma\langle N^{\bar{q}}\rangle_{\Delta y, p_0}] \equiv T_{AB}(\mathbf{b})\sigma\langle N^{B-\overline{B}}\rangle_{\Delta y, p_0}. \quad (8)$$

As discussed in the previous section, the dominant transverse scale in primary production, $p_0 = p_{\rm sat}$, in central rapidities of ultrarelativistic $A+A$ collisions is obtained by solving Eq. (1). Because the predictions of multiplicities at RHIC agreed with the measurements, we do not further tune the initial-state computation from that in Ref. [3], i.e., we use the GRV94 parton densities [59] together with nuclear effects from the EKS98 parametrization [49] and K factors 1.6 (2.3) for RHIC (LHC) based on the NLO analysis of minijet E_T production [50]. Note that the K factors have been shown to vary with the PDFs in a manner that the changes in $\sigma\langle E_T\rangle$ remain small even if newer PDFs were applied [50].

Table I shows the saturation scales, formation times, and pQCD quantities computed at $p_0 = p_{\rm sat}$ for RHIC and LHC in central and nearly central $A+A$ collisions. The centrality selection is simulated as in Ref. [3], by considering a central collision of an effective nucleus $A_{\rm eff} < A$: first, e.g., for 5% most central collisions, we find a maximum impact parameter by taking 5% of the $A+A$ total cross section in a (optical)

TABLE I. The pQCD quantities computed from Eq. (4) with $p_0 = p_{\rm sat}$ in central $A+A$ and in central $A_{\rm eff} + A_{\rm eff}$ collisions at RHIC and LHC corresponding to various centrality cuts and $\Delta y = 1$. The saturation scales from Eq. (1), the corresponding formation times, the number of participants, and the overlap function at $\mathbf{b} = \mathbf{0}$ are shown.

$\sqrt{s}/A$ [GeV]	130		200				5500	
Centrality	0%	5%	0%	5%	10%	15%	0%	5%
A, $A_{\rm eff}$	197	181	197	181	166	153	208	193
$T_{A_{\rm eff}A_{\rm eff}}(0)$ [1/mb]	29.4	26.1	29.4	26.1	23.1	20.6	31.7	28.5
$N_{\rm part}$	377	346	379	347	318	293	407	376
$p_{\rm sat}$ [GeV]	1.08	1.06	1.16	1.15	1.14	1.12	2.03	2.01
τ_0 [fm/c]	0.18	0.19	0.17	0.17	0.17	0.18	0.10	0.10
$\sigma\langle E_T\rangle$ [mbGeV]	65.1	67.0	83.6	85.9	88.3	90.7	468	479
$\sigma\langle N^g\rangle$ [mb]	35.9	37.3	42.9	44.6	46.4	48.2	135	140
$\sum_q \sigma\langle N^q\rangle$ [mb]	4.50	4.66	4.43	4.58	4.75	4.92	6.46	6.66
$\sum_q \sigma\langle N^{\bar q}\rangle$ [mb]	2.65	2.76	2.87	2.98	3.10	3.21	6.14	6.34
$\sigma\langle N\rangle$ [mb]	43.1	44.7	50.2	52.2	54.3	56.3	148	153
$\sigma\langle N_{B-\bar B}\rangle$ [mb]	0.616	0.635	0.520	0.536	0.553	0.570	0.106	0.109

Glauber formulation. Then, we determine $A_{\rm eff}$ by requiring that the number of participants in a central $A_{\rm eff}+A_{\rm eff}$ collision equals the average number of participants computed for the 5% central $A+A$ collisions.

The pQCD calculation of minijet production is a momentum space calculation. To define the initial densities, a connection between the momentum of the minijet and its space-time formation point is needed. At collider energies the nuclei are strongly contracted, $2R_A/\gamma_{\rm cm} \ll 1$ fm, and the typical partons at saturation have a longitudinal spread of $2/(x\sqrt{s}) \sim 1/p_{\rm sat} \ll 1$ fm. We therefore consider the collision region as a point in the longitudinal direction and assume that the rapidity of the minijet coincides with the space-time rapidity of the formation point, $y = \eta = (1/2)\ln[(t+z)/(t-z)]$. The formation (proper) time we take to be the inverse of the saturation scale, $\tau_0 = 1/p_{\rm sat}$. Thus the minijet matter forms along the hyperbola $t = \sqrt{z^2+\tau_0^2}$ with initial longitudinal flow velocity $v_z(\tau_0) = z/t$. The partons in the rapidity interval Δy thus occupy a volume $\Delta V(\tau_0) = A_T \Delta z = \pi R_A^2 \tau_0 \Delta y$ at proper time τ_0.

The average initial energy density, number density, and, as a new element [51,54], the net-baryon number density of the produced parton matter in central $A+A$ collisions are then obtained as follows:

$$\langle\epsilon\rangle = \frac{1}{\Delta V(\tau_0)} E_{T,AA}(\mathbf{0}, p_{\rm sat}, \Delta y, \sqrt{s}) \tag{9}$$

$$\langle n\rangle = \frac{1}{\Delta V(\tau_0)} N_{AA}(\mathbf{0}, p_{\rm sat}, \Delta y, \sqrt{s}) \tag{10}$$

$$\langle n_B\rangle = \frac{1}{\Delta V(\tau_0)} N_{AA}^{B-\overline{B}}(\mathbf{0}, p_{\rm sat}, \Delta y, \sqrt{s}). \tag{11}$$

For nuclei with realistic transverse profiles, however, the saturation scale and thus also the formation time may vary with the transverse coordinate $\mathbf{r} = (x, y)$ [60,61]. We avoid such further modeling here and, following Ref. [3], we consider a constant formation time $\tau_0 = 1/p_{\rm sat}$ and extract the transverse profile for the initial densities by differentiating the overlap function T_{AB} with respect to d^2r. The nucleon-nucleon luminosity for a transverse area element d^2r is $T_A(\mathbf{b}-\mathbf{r})T_B(\mathbf{r})$ and the volume element $dV = dz\, d^2r = \tau\, \Delta y\, d^2r$. These lead to the $\mathbf{r}$-dependent energy density and net-baryon density at $(\tau_0 = 1/p_{\rm sat}, \eta = 0)$ in central $(\mathbf{b} = \mathbf{0})$ $A+A$ collisions,

$$\epsilon(\tau_0, \mathbf{r}) = \frac{dE_T}{\tau_0 d\eta d^2r} = T_A(\mathbf{r})T_A(\mathbf{r})\frac{\sigma\langle E_T\rangle_{\Delta y, p_{\rm sat}}}{\tau_0 \Delta y} \tag{12}$$

$$n_B(\tau_0, \mathbf{r}) = \frac{dN_{AA}^{B-\overline{B}}}{\tau_0 d\eta d^2r} = T_A(\mathbf{r})T_A(\mathbf{r})\frac{\sigma\langle N^{B-\overline{B}}\rangle_{\Delta y, p_{\rm sat}}}{\tau_0 \Delta y}. \tag{13}$$

In Fig. 1 we show the initial energy density in 5% most central Au+Au collisions at $\sqrt{s_{NN}} = 200$ GeV at RHIC and Pb+Pb collisions at $\sqrt{s_{NN}} = 5500$ GeV at the LHC. Notice

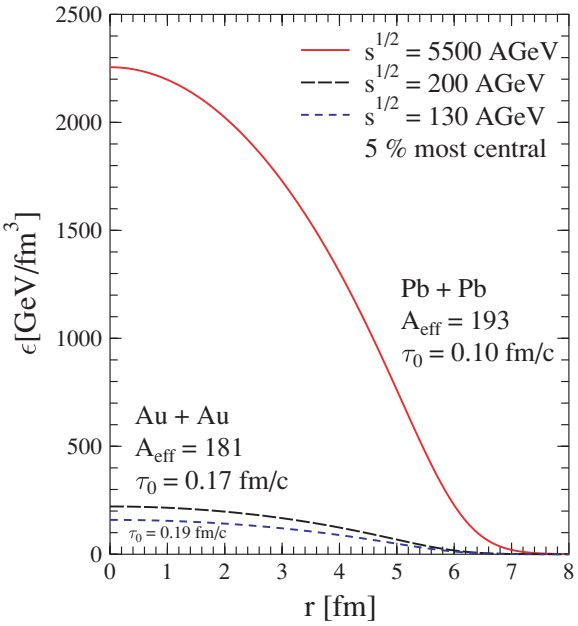

FIG. 1. (Color online) Transverse profile of the initial energy density in an average $A+A$ collision in 5% most central collisions at the LHC (solid line) and RHIC (dashed lines). Formation times and effective nuclei are indicated (see Table I).

the very large densities in the very center of the system. It should, however, be emphasized that because the *volume* near $r \sim 0$ is small, the average energy densities are clearly smaller than those in the center (see Table 1 of Ref. [17]). Another interesting point is the large difference between RHIC and LHC. This is on one hand because of the enhanced gluon production at higher energies (see Table I) and on the other because of the shorter formation time (smaller initial QGP volumes) in the LHC case [see Eq. (12)]. Because the initial transverse size is nearly the same in both cases, the radial pressure gradients are larger at the LHC leading to stronger flow, as discussed in Ref. [62].

The net-baryon number in central rapidity unit, Eq. (8), can now be obtained from Table I. For RHIC, we get $N_{B-\bar{B}} = 16.6$ and 14.0 in 5% most central Au+Au collisions at $\sqrt{s_{NN}} = 130$ and 200 GeV, respectively. For the LHC, we predict $N_{B-\bar{B}} = 3.11$ in 5% most central Pb+Pb collisions at $\sqrt{s_{NN}} = 5500$ GeV.

III. FROM DENSE INITIAL STATE TO DECOUPLED HADRONS

A. The hydrodynamical framework

For the initial state of matter, the pQCD+saturation model provides the initial energy density ϵ and net-baryon number density n_B over a transverse profile at the formation time $1/p_{\rm sat}$ of the system. We make a bold assumption of fast thermalization by taking the thermalization time scale to be the same as the formation time, $\tau_0 = 1/p_{\rm sat}$. Some arguments can be given in favor of this assumption. First, as discussed in Refs. [17,60,63], from the point of view of $\langle\epsilon\rangle$ and $\langle n\rangle$, the saturated (fully gluonic) system indeed looks thermal. This suggests that only elastic collisions causing energy and momentum transfer are needed for thermalization of gluons, number-changing reactions are not essential. Second, the formation time of more energetic (mini-)jets is shorter than the time scale τ_0 associated with the saturation scale, so some secondary interactions have taken place already before the overall formation time. Third, recent studies of plasma instabilities lend support to fast thermalization [64,65] instead of the slower bottom-up thermalization [66]. We also note that we assume full chemical equilibrium and follow the evolution of net-baryon number, which as a conserved quantity should not be sensitive on the details of chemical processes. We do not discuss the dynamics of chemical equilibration of the QGP here. Recent studies on this can be found in Ref. [67].

1. Simplifications: longitudinal scaling flow and azimuthal symmetry

As discussed in Sec. II B, in our minijet description the parton system forms with an initial longitudinal flow velocity $\tanh\theta = v_z = z/t$. Assuming that the expansion maintains this form, the original (3+1)-dimensional problem reduces to (2+1)-dimensional evolution equations for transverse expansion. For central collisions the final state is azimuthally symmetric, leaving only the (1+1)-dimensional equations for radial flow to be solved. In this study we do not consider noncentral collisions that exhibit the interesting phenomena of azimuthally asymmetric flow.

Obviously boost invariance will be broken in real collisions with finite collision energy. However, the assumption of boost invariant flow is still very good in the central rapidity region, as will be argued next. The effects of longitudinal pressure gradients on longitudinal velocity were studied in Ref. [39], where the initial densities were computed from the pQCD minijet rapidity distributions and the initial longitudinal flow velocity was assumed to satisfy the scaling form. Because the radial expansion was neglected, the study [39] overestimates the change of the flow because cooling is slower and system lives longer than with radial flow. The obtained flow deviated only marginally (by a few percents) from the scaling flow at the end of the evolution in the central rapidity region. Similar observation was made in a (2+1)-dimensional analysis at RHIC energy [40].

As the scaling flow does not change much, the transfer of entropy, deposited initially to the central rapidity unit, to larger rapidities due to the development of the longitudinal flow is negligible. Also, the dominant part of the final (thermal) spectra of hadrons comes from the part of the decoupling surface where $|y - \theta| \lesssim 1$, because only a small fraction of particles in thermal bath have large enough energy to end up in central rapidity over a rapidity gap larger than 1. All in all this means that the fragmentation regions, where the assumption of boost invariance breaks down, do not affect significantly the results obtained using scaling flow at the central rapidity.

The question of a rapidity plateau in the final rapidity density dN/dy of hadrons is discussed in more detail in Refs. [21,40]. They show that the plateau would appear in the measured spectra only if the initial densities are flat over a considerable range in space-time rapidity. At RHIC the measured pion spectra are Gaussian [68] and it remains to be seen if a plateau develops at LHC energy. In any case, as argued above, a measured Gaussian rapidity density does not indicate that the description of transverse flow in the central rapidity region based on the assumption of scaling longitudinal velocity is an invalid approximation.

We note that the approximations mentioned above can be relaxed in different ways. There has been a lot of discussion on elliptic flow, see, e.g., a review [69], in which case the approximation of boost invariant flow is retained but the azimuthal symmetry is relaxed. Also, as mentioned above, a genuinely 3+1-dimensional hydrodynamical code for collider energies has been successfully developed [21,22,70–72].

2. Initial transverse flow?

To complete the initial conditions for the hydrodynamic calculation the initial collective transverse motion, $v_r(\tau_0, r)$, must be specified. It can be argued that the change in the number of primary collisions, when going from the center to the edges in the transverse plane, could lead to nonzero initial transverse flow. However, hydrodynamical studies at the SPS energy show that only a very weak initial flow can be tolerated without getting into disagreement with the slopes

of transverse hadron spectra [73]. Because there is no obvious reason for a strong transverse initial flow, we take for simplicity $v_r(\tau_0, r) = 0$.

In Ref. [74] it was found that especially the spectra of protons, at RHIC, are better reproduced if some initial velocity is introduced. However, they use $\tau_0 = 0.6$ fm/c as the thermalization time and argue that the initial velocity arises from prethermal interactions. The velocity they assume is similar in magnitude to that created in hydrodynamical evolution up to $\tau_0 = 0.6$ fm/c if $\tau_0 = 1/p_{\rm sat} \sim 0.2$ fm/c is assumed, as we do. Whether or not the system is fully thermalized at $\tau_0 = 1/p_{\rm sat}$, this early starting of hydrodynamical evolution can effectively describe the initial buildup of transverse flow as a result of the collisions that lead to thermalization.

3. Equation of State

Another key input in the hydrodynamic studies is the equation of state, $P = P(\epsilon, n_B, n_S)$, specifying pressure as a function of energy density, net-baryon number density, and net strangeness density. Because strong interactions conserve strangeness, the total strangeness in the expanding matter of a heavy-ion collision is zero. In principle nonzero strangeness spots could be generated in the matter through fluctuations but we assume that the net strangeness vanishes locally. This condition is imposed on the EOS and we write simply $P(\epsilon, n_B)$ for $P(\epsilon, n_B, n_S = 0)$. With the initial conditions considered here, the effects of n_B on pressure are negligible, which we have checked, and for the hydrodynamical simulations we use $P(\epsilon, n_B = 0)$ for simplicity. However, when calculating the final hadron spectra the value of n_B and the condition $n_S = 0$ are essential in determining the baryon and strangeness chemical potentials that enter the thermal distributions of hadrons [see Eqs. (16) and (17) ahead]. When hydrodynamic simulations are converted to hadron spectra, the EOS in full (ϵ, n_B) plane is used.

In principle the EOS can be obtained from lattice QCD. A full EOS with finite quark masses and finite baryochemical potential μ_B is, however, not yet available. It is expected that for small values of μ_B relevant at central rapidity region at collider energies the transition from hadron gas to parton matter is a rapid crossover [75]. For the recent progress on lattice calculations, see, e.g. [76,77]. From the point of view of radial hydrodynamic flow the difference between a weak first-order transition and a rapid crossover is qualitatively not very significant as long as the EOSs are similar away from the transition region. Because we would like to be able to include the dependence of spectra on quantum numbers through the chemical potentials, we use in calculations an EOS with ideal QGP in the high-temperature phase and a hadron resonance gas (HRG) below the transition. For these phases it is easy to include the chemical potentials into the EOS.

A first-order transition is implemented by introducing a bag constant B into the QGP phase and connecting the two phases via the Maxwell construction. The inclusion of resonances in the hadron phase mimics the effects of both attractive and repulsive interactions between hadrons reasonably well [78]. We include all hadron and hadron resonance states up to $m = 2$ GeV. A detailed account of constructing such an EOS can be found, e.g., in Ref. [24]. With $N_f = 3$ we set the bag constant B to be $B^{1/4} = 239$ MeV, giving $T_c = 165$ MeV for the transition temperature.

Another way to construct an EOS would be to parametrize the $n_B = 0$ lattice results above the QCD phase transition [79] and join it smoothly with HRG EOS at T_c. We have checked that hadron p_T spectra obtained with such an EOS do not differ significantly from those obtained with the bag model QGP-HRG EOS.[1] In this article, we shall show results with the QGP-HRG EOS only.

4. Hydrodynamic equations

With the longitudinal scaling flow and the assumed azimuthal symmetry, the transverse velocity and thermodynamic densities become functions of proper time τ and transverse coordinate r only: $v_r = v_r(\tau, r), \epsilon = \epsilon(\tau, r), n_B = n_B(\tau, r), P = P(\tau, r), \ldots$. The hydrodynamic equations are

$$\partial_\mu T^{\mu\nu}(x) = 0 \qquad \text{and} \qquad \partial_\mu j_B^\mu(x) = 0, \tag{14}$$

where

$$T^{\mu\nu} = (\epsilon + P)u^\mu u^\nu - P g^{\mu\nu} \qquad \text{and} \qquad j_B^\mu = n_B u^\mu$$

are the stress-energy tensor and the net-baryon current. With the above assumptions Eq. (14) simplify to 1+1-dimensional forms [16,81]. Given an EOS in the form $P = P(\epsilon, n_B = 0)$ with $n_S = 0$ as discussed above, they can be easily solved numerically.

5. Decoupling and decays

In hydrodynamic description the final-state hadron spectra are obtained by folding the thermal motion with the fluid motion on a decoupling surface $\sigma(\tau, r)$, which we define from the condition $T(\tau, r) = T_{\rm dec}$. Given the velocity field and the thermodynamic densities, we calculate the thermal spectra of hadrons h by using the Cooper and Frye prescription [82]

$$\begin{aligned}
\pi \frac{dN^h}{d^3\mathbf{p}/E} &= \frac{dN^h}{dy dp_T^2} \\
&= \pi \int_\sigma d\sigma_\mu(x) p^\mu f_h[x, p; T(x), \mu_h(x)] \qquad (15) \\
&= \frac{g_h}{2\pi} \sum_{n=1}^{\infty} (\pm 1)^{n+1} \int_\sigma r\tau e^{n\mu_h(\tau,r)/T(\tau,r)} \\
&\quad \left[-p_T I_1\left(n\gamma_r v_r \frac{p_T}{T}\right) K_0\left(n\gamma_r \frac{m_T^h}{T}\right) d\tau \right. \\
&\quad \left. + m_T^h I_0\left(n\gamma_r v_r \frac{p_T}{T}\right) K_1\left(n\gamma_r \frac{m_T^h}{T}\right) dr \right], \qquad (16)
\end{aligned}$$

where $\mu_h = B_h\mu_B + S_h\mu_S$ is the chemical potential, g_h the spin degeneracy factor and $m_T^h = \sqrt{m_h^2 + p_T^2}$ the transverse mass of the hadron of type h. The last form, Eq. (16), holds for the boost invariant cylindrically symmetric radial flow. The upper (lower) sign is for mesons (baryons) and

[1] For a recent study on the EOS effects on elliptic flow, see Ref. [80].

$\gamma_r = (1 - v_r^2)^{-1/2}$. Also, the condition $\mu_h(\tau, r) < m_h$ must always be satisfied for mesons and, for the expansion in Eq. (16) to hold, also for baryons.[2] This is the case here.

Chemical potentials for baryon number and strangeness, μ_B and μ_S, are obtained on the decoupling surface by expressing the calculated net-baryon density and the strangeness neutrality in terms of free-particle densities:

$$n_B = \sum_h B_h n_h(T, \mu_h) \quad \text{and} \quad 0 = \sum_h S_h n_h(T, \mu_h), \qquad (17)$$

where B_h is the baryon number and S_h the strangeness of a hadron h.

The preferred value $T_{\rm dec} = 150$ MeV is extracted on the basis of RHIC data [54] but we will also show the sensitivity of our results to $T_{\rm dec}$. The thermal spectra are calculated for all hadrons and resonances included in the hadronic EOS.

To obtain final spectra which can be compared with the experimentally observable ones, we consider all strong and electromagnetic two- and three-body decays of hadron resonances, with branching ratios obtained from Ref. [83]. Decay kinematics is discussed in details, e.g., in Ref. [84]. Also feed-down effects from weak decays of hyperons are discussed.

B. Properties and effects of collective motion

1. Longitudinal flow and transfer E_T

The effects of collective motion arise from the thrust due to collisions among produced particles, described by pressure in the hydrodynamic treatment. The most important overall effect of the rapid longitudinal expansion is to transfer a large fraction of (transverse) energy from central region to longitudinal motion, see Ref. [39] for a discussion. The measured final transverse energy at RHIC is roughly a third of what is predicted by pQCD+saturation, and the same is expected to happen at the LHC as well [3]. At the same time, however, the number of calculated minijets is quite close to the final multiplicity. In the hydrodynamic approach the approximate conservation of the number of particles is a consequence of the (approximate) conservation of entropy. The initial energy density, or equivalently, because instant thermalization is assumed, the initial entropy density obtained from pQCD+saturation thus essentially determines the final multiplicity [17].

Longitudinal expansion alone would cool and dilute the matter to free hadrons. However, with the very large initial densities created at collider energies, the time needed for this, the longitudinal time scale, is so long that effects in the transverse direction cannot be neglected. From the point of view of the transverse energy at central rapidities we have two opposing effects: In the longitudinal expansion the large initial thermal energy is transferred to longitudinal motion and the transverse energy is reduced. However, the buildup of transverse flow limits this transfer and part of the initial thermal energy is converted to the transverse collective motion and thus to the measured transverse energy. Even though the fraction of energy transfer into transverse collective motion is much less than into longitudinal, it produces an effect that is seen as an increase in the average transverse momentum (see, e.g., Ref. [85]) or in the effective temperature, measured as the inverse of the slope of the spectra.

2. Properties of transverse flow

The main overall effect of transverse flow in the hydrodynamic evolution is a more rapid cooling, leading to clearly shorter lifetime of the thermal system than with the longitudinal expansion alone. This is illustrated in Figs. 2–5, which show our results for the hydrodynamic spacetime evolution in the framework discussed above. Figures 2 and 3 are for the RHIC and the next two for the LHC. Fig. 2 and 4 show the flow lines in the (τ, r) plane, and Fig. 3 and 5 the transverse velocity contours. The phase boundaries QGP-mixed phase (MP) and MP-HRG are shown by the thick curves. Also drawn are two isotherms corresponding to $T_{\rm dec} = 150$ MeV and $T_{\rm dec} = 120$ MeV.

It is interesting to compare the QGP lifetime at $r = 0$ with that in a system subject to longitudinal scaling flow only. Such a system would cool down from ϵ_0 to the critical energy density of QGP, $\epsilon_c = 1.93$ GeVfm^{-3} at $\tau_c = \tau_0(\epsilon_0/\epsilon_c)^{3/4}$. For the maximum values from Fig. 1, $\epsilon_0 \approx 220$ GeVfm^{-3} at RHIC and 2260 GeVfm^{-3} at the LHC, and for the initial times from Table I, we get $\tau_c = 6.0$ fm/c at RHIC and $\tau_c = 20$ fm/c at the LHC. These are to be contrasted with $\tau_c(r = 0) \approx 5$ fm/c at RHIC and 7.5 fm/c at the LHC in Figs. 2–5. The effects of transverse expansion thus become important already at the QGP phase at the LHC.

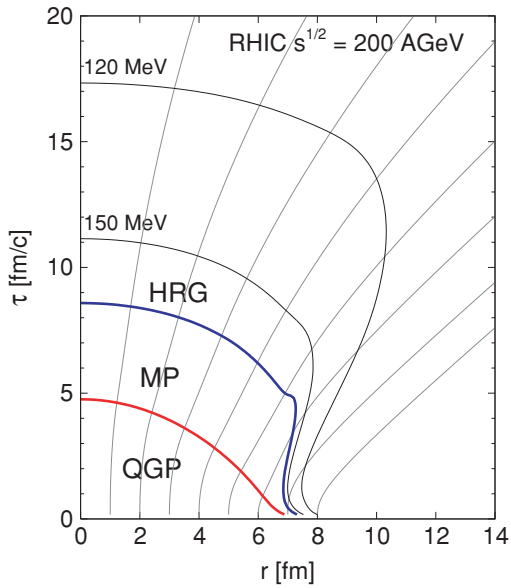

FIG. 2. (Color online) The phase boundaries and the two decoupling curves studied, $T_{\rm dec} = 150$ and 120 MeV, with selected flowlines in the plane of proper time τ and transverse variable r in 5% most central Au+Au collisions at $\sqrt{s_{NN}} = 200$ GeV.

[2]For $\mu_h(\tau, r) > m_h$, regions with $\mu_h(\tau, r)$ bigger or smaller than m_T^h must be treated separately.

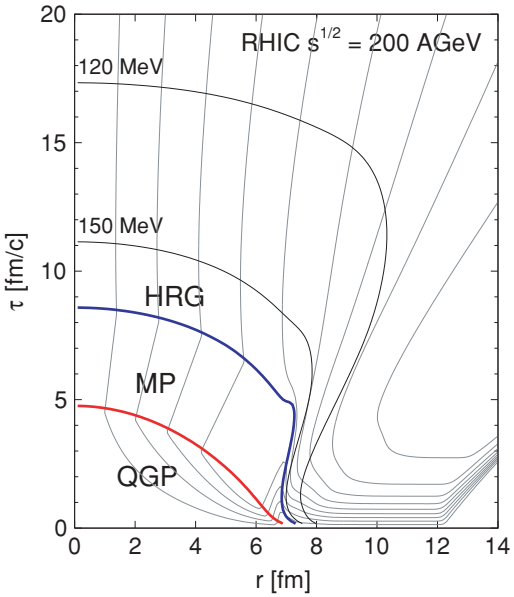

FIG. 3. (Color online) Contours of transverse velocity v_r in the (τ, r)-plane in 5% most central Au+Au collisions at $\sqrt{s_{NN}} = 200$ GeV. Reading from left to right, $v_r = 0.1, 0.2, \ldots, 0.9$.

The evolution of the transverse flow is clearly seen in these figures. The flow lines $r = r(t)$ (at $z = 0, \tau = t$) in Figs. 2 and 4 depict how a fluid element in a given differential interval in transverse variable at τ_0 moves radially outward. There is no entropy-flux across the flow lines so we get an idea of where the initial multiplicity goes (once the transverse volume is properly accounted for). The slope of the flow line, $dr(t)/dt$, gives the local radial flow velocity $v_r(r(t), t)$. Thus, the bending of the flow lines seen in the QGP and HRG phases indicates acceleration of the fluid. The straight flow lines observed in the MP in turn indicate a constant pressure and no acceleration.

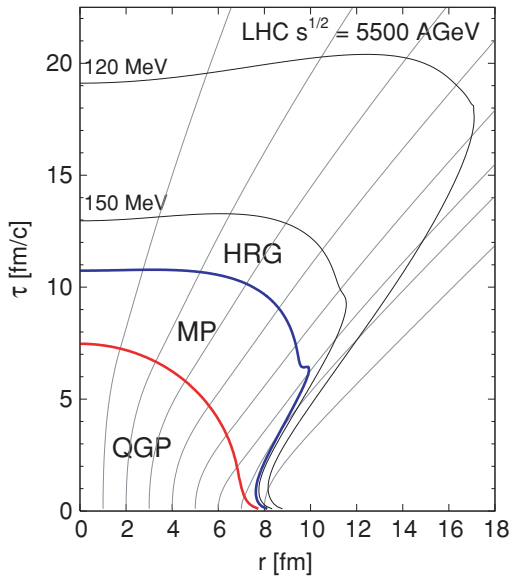

FIG. 4. (Color online) As in Fig. 2 but for 5% most central Pb+Pb collisions at $\sqrt{s_{NN}} = 5500$ GeV.

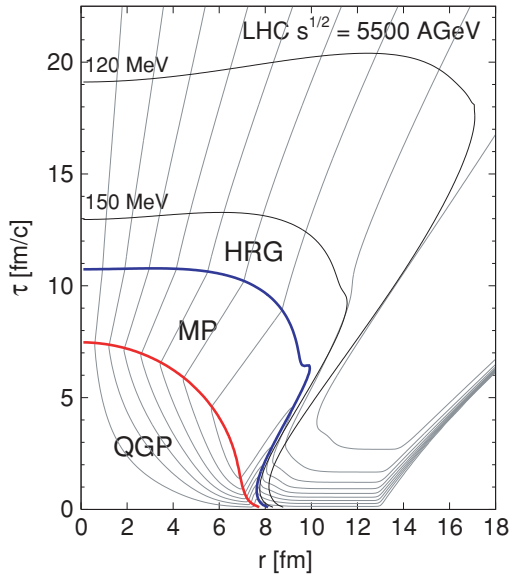

FIG. 5. (Color online) As in Fig. 3 but for 5% most central Pb+Pb collisions at $\sqrt{s_{NN}} = 5500$ GeV.

The corresponding constant velocity contours at RHIC and LHC, which, reading from left to right, are $v_r = 0.1, 0.2, \ldots, 0.9$, are shown in Figs. 3 and 5. The velocity contours illustrate how the deflagration wave penetrates into the fireball as the radial pressure gradient pushes the matter to collective motion. A kink at the boundary of QGP and mixed phase (MP) results from disappearance of pressure gradients in the MP. As there is no acceleration in the MP, the matter continues to flow with radial velocity obtained already in QGP. The reappearance of pressure gradients, when matter enters from MP to hadron gas phase, is seen as a kink in the velocity contours at the phase boundary.

The dense bundle of velocity contours starting around $r \gtrsim 10$ fm results from the treatment of the nuclear surface. Even though we take the densities smoothly to zero, the expansion is essentially to vacuum and the velocities approach the velocity of light. This region has no consequences for any physical observables, because it is outside the decoupling surface in a region with vanishingly small densities.

Because the larger energy density leads to larger pressure gradients at LHC than at RHIC, the transverse flow at LHC grows also much stronger than at RHIC. This is seen both in the larger radial extent of the decoupling curve and the larger values reached in transverse velocity at decoupling. We next discuss how this affects qualitatively the transverse spectra of hadrons.

3. Effects of transverse flow on hadron spectra

It is well known that transverse flow broadens the m_T spectra of hadrons and, because heavier particles obtain a larger momentum increase from the collective flow velocity, the effective temperature T_{eff}, defined as the inverse of the m_T slope of the logarithm of a spectrum, and the average

transverse momentum

$$\langle p_T^h \rangle \equiv \frac{\int dp_T\, p_T\, dN^h/dydp_T}{\int dp_T\, dN^h/dydp_T}, \tag{18}$$

increase with particle mass. Before discussing the actual results, we demonstrate the effects of flow in a simplified system of homogeneous cylinder with radius R, which decouples at $\tau = \tau_f = \text{const}$. In this case, if $\mu_h = 0$, the Cooper-Frye formula (5) reduces to[3]

$$\frac{dN}{dydm_T^2} = \frac{g}{2\pi}\tau_f m_T \sum_{n=1}^{\infty}(\pm 1)^{n+1} \times \int_0^R dr\, r I_0\left(n\gamma_r v_r \frac{p_T}{T}\right) K_1\left(n\gamma_r \frac{m_T}{T}\right), \tag{19}$$

where the index h has been suppressed. Integration over r is trivial if $v_r = \text{const}$. In particular, if no transverse flow is present, $v_r = 0$, Eq. (19) simplifies to

$$\frac{dN}{dydm_T^2} = \frac{g}{4\pi}\tau_f R^2 m_T \sum_{n=1}^{\infty}(\pm 1)^{n+1} K_1\left(\frac{nm_T}{T}\right) \overset{m_T/T \gg 1}{\longrightarrow} \frac{g}{\sqrt{32\pi}}\tau_f R^2 \sqrt{m_T T}\, e^{-m_T/T}, \tag{20}$$

where also the asymptotic behavior at large m_T/T is indicated.

The upper set of curves in Fig. 6 is obtained using Eq. (20), i.e., there is no transverse flow. In that case, spectra of all particles, here three spin-0 bosons with masses $m = 140$, 494, and 938 MeV, are the same except that their m_T- spectra start from particles mass (different curves are made visible by multiplying the $m = 494$ and 938 MeV curves with 1.2 and 0.8, respectively). This is known as the m_T scaling. The overall normalization of the curves is left free, as we consider now the slopes only.

Nonzero transverse velocity breaks the m_T scaling at $p_T \lesssim m$. This is illustrated by the lower set of curves in Fig. 6 using constant transverse flow $v_r = 0.6$. The asymptotic behavior of Eq. (19) at $m_T/T \gg 1$ shows an exponential factor $\exp\{-m_T/T_{\text{eff}}\}$ with $T_{\text{eff}} = \sqrt{(1+v_r)/(1-v_r)}T$. Thus the m_T scaling of the slopes is recovered asymptotically. In the example of Fig. 6 with $v_r = 0.6$, $T_{\text{eff}} = 2T$. This explains why the slopes of the spectra are nearly the same in the cases $T = 220$ MeV, $v_r = 0$ and $T = 110$ MeV, $v_r = 0.6$.

This simple study very clearly demonstrates the role of the transverse flow in the properties of transverse spectra of hadrons, and the necessity to understand the dynamical evolution of the transverse flow in detail for proper interpretation of measured slopes.

Let us turn to discuss the flow in more realistic hydrodynamical simulations, presented in Figs. 2–5. There is an interesting interdependence between the EOS, spacetime evolution of the flow, and the slopes of thermal hadron spectra. As long as a phase transition is included in the EOS, the strength

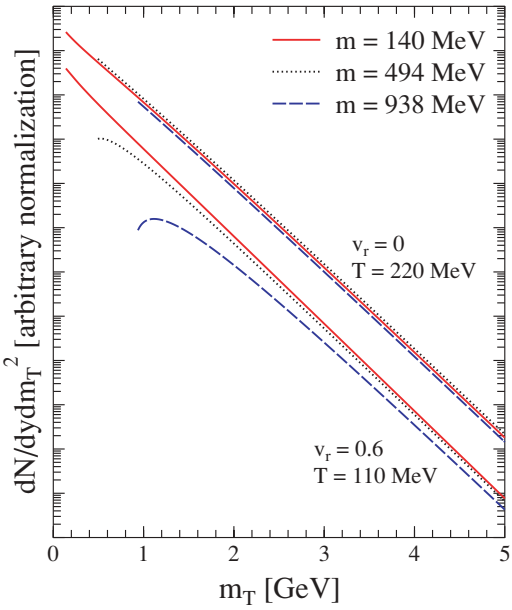

FIG. 6. (Color online) An example of how transverse flow affects the slopes of hadron spectra in a simplified system that decouples at a constant proper time and a constant radial flow velocity v_r. Two sets of spectra, computed from Eq. (19) but leaving the overall normalization arbitrary, are shown for bosons of masses $m = 140$ (solid lines), 494 (dotted), and 938 MeV (dashed). The upper set of curves, where $v_r = 0$ and temperature $T = 220$ MeV, shows m_T scaling (for better visibility, the curves for 494 and 938 MeV are multiplied by 1.2 and 0.8, respectively). In the lower set $v_r = 0.6$ and $T = 110$ MeV. At small m_T, the m_T scaling is broken because of a nonzero v_r, but the spectral slopes are similar to the upper set at $m_T \gg T, m$.

of final flow on the decoupling surface, of fixed decoupling temperature, is not very sensitive to the number of hadron resonance states included in the hadronic phase, whereas the actual spacetime evolution of the system may vary quite significantly. This can be understood as follows: Reduction of the hadronic states in the EOS leads to a stronger phase transition between the QGP and HRG, i.e., latent heat as well as entropy ratio between the two phases increase. This makes the deflagration from mixed phase to HRG stronger. It increases also the pressure gradients in HRG because the reduction of hadronic states leads to a larger sound velocity c_s and the pressure is given by $p = c_s^2\varepsilon$. As discussed in Ref. [54], the energy release from heavy resonance states significantly slows down the decrease of temperature during the evolution. Thus, when we decrease the number of hadron resonance states in HRG, it results in faster development of flow and drop in temperature, leading to a shorter lifetime of the matter. For larger number of hadron resonance states the flow grows more slowly but the energy release from heavy resonances leads to longer time for the flow to build up. In practice these effects compensate each other and as a result, the slopes of the spectra are relatively independent of the hadron content of the EOS.

There is, however, a relatively strong dependence of the effective temperature, the inverse of spectral slope, on the decoupling temperature [54] once the hadron content of

[3]This form, Eq. (19), was used in a blast-wave fit [86], where $v_r = (r/R_A)v_{\max}$ was assumed and where the parameters T and $v_{\max}$ were fitted to reproduce the *shape* of the final hadron spectra.

the EOS is fixed. In Sec. V, we shall illustrate the variation of the hydrodynamical results in the range of decoupling temperatures $T_{\rm dec} = 150 \ldots 120$ MeV. In particular, with the given pQCD+saturation initial state and with the relatively steep initial transverse profile, we show that the RHIC spectra favor the higher $T_{\rm dec}$ both at $\sqrt{S_{NN}} = 130$ and 200 GeV.

IV. HADRONS FROM FRAGMENTATION OF HIGH-p_T PARTONS

A. pQCD framework for computing high-p_T spectra

Inclusive hadron spectra in high-energy hadronic or nuclear collisions are computable in terms of collinearly factorized partonic hard parts (cross sections in LO) $\hat{\sigma}_{ij\to f+k}$, parton distribution functions (PDFs) $f_{i/A}$ and $f_{j/B}$, and fragmentation functions (FFs) $D_{f\to h}$, schematically as

$$d\sigma^{AB\to h+X} = \sum_{ijk} f_{i/A} \otimes f_{j/B} \otimes \hat{\sigma}_{ij\to f+k} \otimes D_{f\to h}, \qquad (21)$$

where the fragmentation function, $D_{f\to h}$, gives the average multiplicity of h hadrons produced from a parton f. The NLO pQCD computation [87,88], which requires NLO PDFs and FFs as well, provides a successful description of the high-p_T spectra in $p+\bar{p}$ collisions at collider energies. Also the leading-order considerations are useful and have been shown to agree quite well with the data in the large-p_T region, once the overall normalization, the K factors, are extracted from the data [18]. We make use of the latter: By applying the energy-dependent K factors of Ref. [18] and including in the analysis also the recent $p+p$ data from RHIC [6], we determine the K factors at $\sqrt{s} = 130$ and 200 GeV and also, through extrapolation, at the LHC energy $\sqrt{s} = 5500$ GeV. Armed with these and by including nuclear effects in the PDFs according to the EKS98 parametrization [49], we compute the baseline pQCD spectra of high-p_T hadrons for nearly central $A+A$ collisions at RHIC and LHC. We do not make further modeling to account for the Cronin effect or any intrinsic k_T effects in the PDFs or in the FFs [89–91].

As presented in detail, e.g., in Ref. [18], inclusive spectrum of the high-p_T hadrons in $A+A$ collisions at an impact parameter **b** in the collinearly factorized LO pQCD formalism becomes

$$\frac{dN^h_{AA}(\mathbf{b})}{dm_T^2 dy} = K(\sqrt{s}, Q, \mu_F) \cdot J(m_T, y) \times \sum_f \int_{z_{\rm min}}^1 \frac{dz}{z^2} D_{f\to h}\left(z, \mu_F^2\right) \frac{dN^f_{AA}(\mathbf{b})}{dq_T^2 dy_f}, \qquad (22)$$

where $f = g, u, d, \ldots$ labels the different parton types and h those of hadrons. The transverse momentum and rapidity of the produced parton are $q_T \geqslant q_{T0}$ and y_f, whereas m_T and y are the transverse mass and rapidity of the hadron. The hadron of fractional energy $z = E_h/E_f$ is assumed to form collinearly with its mother parton. Thus the kinematic variables are related as

$$q_T = \frac{p_T}{z} J(m_T, y), \quad J(m_T, y) = \left(1 - \frac{m^2}{m_T^2 \cosh^2 y}\right)^{-1/2}$$
$$y_f = \operatorname{arsinh}\left(\frac{m_T}{p_T} \sinh y\right), \quad \text{and} \qquad (23)$$
$$\frac{2m_T}{\sqrt{s}} \cosh y \leqslant z \leqslant \min\left[1, \frac{p_T}{q_{T0}} J(m_T, y)\right].$$

We shall here apply the KKP fragmentation functions [92] with a scale choice $\mu_{\rm F} = p_T$. The inclusive spectra for the production of parton type f is obtained at LO from Eq. (2) by integration [18],

$$\frac{dN^f_{AA}(\mathbf{b})}{dq_T^2 dy_f} = T_{AA}(\mathbf{b}) \frac{d\sigma^f_{AA}}{dq_T^2 dy_f} = T_{AA}(\mathbf{b}) \int dy_1 dy_2 \sum_{\langle kl\rangle} \frac{d\sigma^{AB\to kl+X}}{dq_T^2 dy_1 dy_2} [\delta_{kf}\delta(y_f - y_1) + \delta_{lf}\delta(y_f - y_2)] \frac{1}{1+\delta_{kl}}, \qquad (24)$$

where T_{AA} is the nuclear overlap function from Eq. (7). We define the nuclear PDFs by including the x- and Q-dependent EKS98 nuclear modifications [49] on top of the the CTEQ5 [93] PDFs of the free proton. Isospin effects in the nPDFs are accounted for in the same manner as in Ref. [49]. The factorization/renormalization scale is again chosen as $Q = q_T$.

The factor $K(\sqrt{s}, Q, \mu_{\rm F})$ controlling the overall normalization of the pQCD fragmentation spectrum in Eq. (22), is here a phenomenological parameter that accounts for all higher-order contributions in the partonic hard parts, PDFs and FFs (as well as for any scale dependence arising from a truncation of the perturbation series). This K factor can be determined on the basis of the $p+\bar{p}$ and $p+p$ data. It should be emphasized that K depends not only on $\sqrt{s}$ but also the choices for the scales Q and $\mu_{\rm F}$ and on the PDF and FF sets used. The K factors for the parameters specified above have been obtained in Ref. [18] for various cms energies by using the data from the AFS [94], UA1 [95], UA1 MIMI [96], and CDF [97] experiments. These results are shown in Fig. 7. As new input, we now include also the K factor corresponding to the recent STAR charged-particle data from $p+p$ collisions at $\sqrt{s} = 200$ GeV at RHIC [6]. The inner error bars shown correspond to the statistical errors of our K-factor analysis [18], for the outer error bars these have been added in quadrature with the systematic errors of the data.[4] As discussed in detail in Ref. [18], the best agreement between the shapes of the computed and measured spectra is obtained by construction at $p_T \gtrsim 4 \ldots 5$ GeV but the overall agreement is surprisingly good over a wider p_T range.

Based on the systematic decrease of $K(\sqrt{s})$ in Fig. 7, we extrapolate our LO pQCD reference spectra to the LHC by making the following two simple parametrizations to the

[4]For CDF and UA1 MIMI we assume a 15% systematic error.

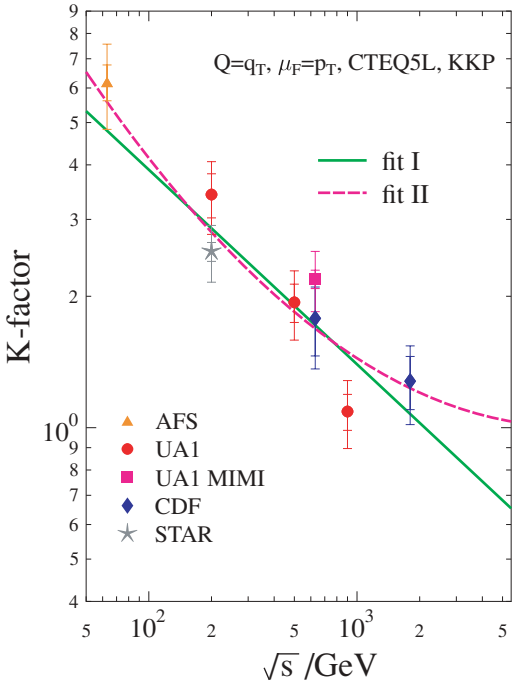

FIG. 7. (Color online) The K factors obtained from fitting the computed leading-order high-p_T hadron spectra to the $p+\bar{p}$ and $p+p$ data. The fit I to $\ln K$, which is linear in $\ln\sqrt{s}$, see Eq. (26), is shown by the solid line and the quadratic fit II by the dashed curve. The parameter values and error bar specifications can be found in the text.

obtained K factors,

$$\text{I}: \quad \ln K = a + b\ln\sqrt{s} \tag{25}$$

$$\text{II}: \quad \ln K = a + b\ln\sqrt{s} + c(\ln\sqrt{s})^2, \tag{26}$$

where $\sqrt{s}$ is in GeV. We get $(a, b) = (3.4131; -0.44569)$ for the fit I with $\chi^2 = 43.2$, and $(a, b, c) = (5.6206; -1.2139; 0.065615)$ with $\chi^2 = 40.6$ for the fit II. Both fits are also shown in Fig. 7. Because systematic errors are not given for all cases, only statistical errors (see Ref. [18]) are considered in these fits. At RHIC energies the K factors are not sensitive to the assumed form of parametrization (see Fig. 7). For the pQCD spectra at the LHC, we give an uncertainty band corresponding to the different K factors obtained from these fits. We note that a similar fit procedure was introduced also in [91] but modeling in also a Gaussian smearing from intrinsic-k_T effects.

B. Energy losses for hard partons

To study the interrelation of the hydrodynamic and pQCD hadron spectra at RHIC and at the LHC more meaningfully, we also consider effects induced by the partonic energy losses to the high-p_T pQCD fragmentation spectra. First we note that the nuclear effects in the PDFs, which are constrained to reproduce the nuclear DIS data through global DGLAP fits, are not responsible for the factor ~ 5 suppression discovered in the hadron spectra in central Au+Au collisions at RHIC at $p_T \gtrsim 5$ GeV. In fact, as shown in Ref. [18], the nuclear modifications slightly (by 0...15%) *enhance* the spectra below $p_T \approx 13$ GeV relative to $p+p$. The energy losses we consider within the framework given in Refs. [19,20], by folding quenching weights with parton production cross sections and FFs, schematically written as

$$d\sigma^{AA\to h+X} = \sum_{ijk} f_{i/A} \otimes f_{j/A} \otimes \hat{\sigma}_{ij\to f+k} \otimes P_f(\Delta E, L, \hat{q}) \otimes D_{f\to h}. \tag{27}$$

The quenching weights, $P_f(\Delta E, L, \hat{q})$, are generalized probabilities for a hard parton f to lose an amount ΔE of its original energy through radiation induced by the medium over a path length L. The transport coefficient $\hat{q}$ corresponds to the average transverse-momentum squared per unit pathlength gained by the hard parton in traversing the matter. The transport coefficient reflects the average number and energy densities of the system as $\hat{q} \propto n \sim \epsilon^{3/4}$ [98], and it controls the energy loss.

We compute the pQCD spectra subject to energy losses according to the formulation given in Sec. II B of Ref. [19]. We do not repeat the discussion here, but for illustrative purposes we note that when the energy losses are taken into account, the analog of Eq. (22) can be written in terms of medium-modified fragmentation functions [99] for central $A+A$ collisions as

$$\frac{dN^h_{AA}(\mathbf{0})}{dp_T^2 dy} = K \cdot J(m_T, y) \sum_f \int \frac{dz}{z^2} \int dr\, r\, d\phi D^{(\text{med})}_{f\to h} \times \left(z, r, \phi, p_T^2\right) \cdot [T_A(r)]^2 \frac{d\sigma^f_{AA}}{dq_T^2 dy}, \tag{28}$$

where the hard parton's original transverse momentum is $q_T = J(m_T, y)p_T/z$, the distance of the hard parton's production point from the center of the transverse plane is $r = |\mathbf{r}|$, and the azimuthal angle between the hard parton's original transverse momentum $\mathbf{q_T}$ and the transverse vector $\mathbf{r}$ is ϕ. The medium-dependent fragmentation functions are defined as [99]

$$D^{(\text{med})}_{f\to h}\left(z, r, \phi, p_T^2\right) = \int \frac{d\varepsilon}{1-\varepsilon} P_f[\varepsilon, L(r,\phi), \hat{q}] D_{f\to h}\left(\frac{z}{1-\epsilon}, p_T^2\right), \tag{29}$$

where $\varepsilon = \Delta E/E_i$ is the energy fraction lost by the hard parton f and the quenching weights are computed from those of Ref. [20]. The length L traversed by the parton in the QGP now depends on the transverse location of production and on the angle ϕ. In determining the path lengths L, a homogeneous transverse disk profile of a radius R_A is assumed [19].

In what follows, we compute the spectra with normalization fixed by the K factors determined above. As discussed in Ref. [19], the obtained spectra are not sensitive to the (average) lifetime of the plasma once it is of 4–5 fm/c or more, which is the case here (see Figs. 2 and 4). In particular, in 5% most central Au+Au collisions at $\sqrt{s_{NN}} = 200$ GeV we apply a large time-averaged transport coefficient $\hat{q} = \hat{q}_{200} = 10\ \text{GeV}^2/\text{fm}$, which was extracted in Ref. [19] from the RHIC data in the region $p_T \gtrsim 5$ GeV. For the other energies and A_{eff}

studied, we scale $\hat{q}$ according to

$$\hat{q}(A, \sqrt{s_{NN}}) = \hat{q}_{200}(A/181)^{0.383}(\sqrt{s_{NN}}/200\,\mathrm{GeV})^{0.574} \quad (30)$$

on the basis of the average number density scaling of our QGP initial conditions, as discussed in Ref. [19].

The quenching weights applied here are computed in the eikonal high-energy approximation where the lost energy ΔE can in principle be arbitrarily large. Thus, with finite kinematics it may happen that the probabilities are not always normalized properly to unity within the parton energy range available,

$$\int_0^{q_T \cosh y} d(\Delta E) P_f(\Delta E, \hat{q}, L) < 1. \quad (31)$$

Although too-large suppression can follow from this loss of probability, this computation, however, gives us a lower limit of the hadron spectra. An estimate of the upper limit can be obtained by reweighting the quenching weights so that probability conservation is always enforced (see Refs. [19,100]). In our results for the high-p_T spectra (Figs. 8–11, 13, 15, and 16), we give an uncertainty band corresponding to these two limits.

V. RESULTS

We shall next compare the hydrodynamical and pQCD-based results with the measured spectra in central and nearly central Au+Au collisions at RHIC and make an extrapolation to Pb+Pb at the LHC. At RHIC, the hydrodynamic spectra cover the small-p_T region up to a few GeV and the pQCD spectra the region at $p_T \gtrsim 4 \ldots 5$ GeV. The pQCD calculation of the hadron spectra is expected to become less accurate at the lower end, below $p_T \lesssim 4$ GeV (see Ref. [18]), and similarly the uncertainty in the tails of hydrodynamic results grows with p_T. However, as will be seen below, the difference in the slopes of the spectra from the hydrodynamic and the pQCD calculations with energy losses in particular, is rather large. This should reduce the uncertainty in the crossing of two contributions at the LHC in particular, where the hydrodynamic spectra are shown to dominate over a larger p_T region than at RHIC.

A. Comparison with RHIC data

We first compare our results with the experimental data collected by STAR [6,7,101,102], PHENIX [8,9,103–106], PHOBOS [10,107], and BRAHMS [11,108,109] Collaborations for the most central bins in Au+Au collisions at $\sqrt{s_{NN}} =$ 130 and 200 GeV. As explained in Sec. II B, the centrality selection is accounted for by considering central $A_{\mathrm{eff}}+A_{\mathrm{eff}}$ collisions.

1. Transverse-momentum spectra

First, we consider the p_T spectra of charged particles measured at central pseudorapidities η. Figure 8 shows the data taken in 5% most central Au+Au collisions at $\sqrt{s_{NN}} =$ 130 GeV by STAR [7] and PHENIX [9] Collaborations. Similarly, Fig. 9 shows the spectra of charged particles at $\sqrt{s_{NN}} = 200$ GeV measured by PHENIX [8], STAR [6], PHOBOS [10], and BRAHMS [11] Collaborations. The hydrodynamic results are computed accordingly [3], using two different decoupling temperatures, $T_{\mathrm{dec}} = 150$ MeV (solid line) and 120 MeV (dashed line). In addition to the strong and electromagnetic decays, we have here included also the feed down from the weak decays of hyperons, which affects the total number of charged pions, kaons, and (anti-)protons on a few-percent level (see Table III ahead). Note that our hydrodynamical results are for 5% most central collisions, whereas some data are taken in larger centrality bins, as indicated in the figures.

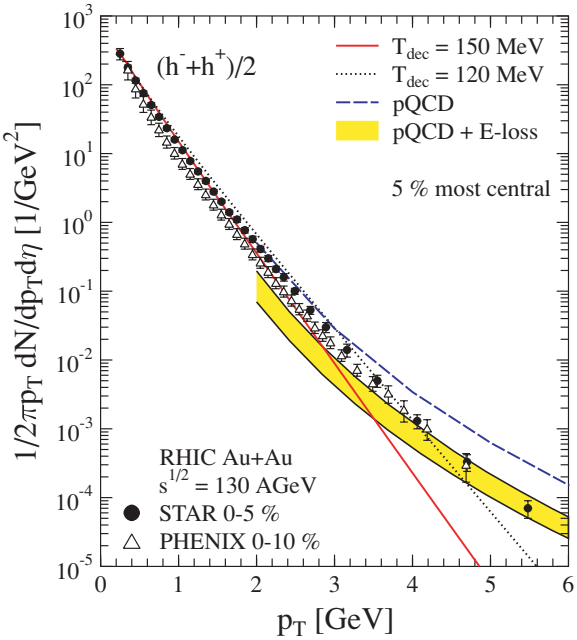

FIG. 8. (Color online) Transverse-momentum spectra of charged particles at $\eta = 0$ (averaged over $|\eta| \leqslant 0.1$) in 5% most central Au+Au collisions at $\sqrt{s_{NN}} = 130$ GeV. Our hydrodynamic results are shown for $T_{\mathrm{dec}} = 150$ MeV (solid line) and $T_{\mathrm{dec}} = 120$ MeV (dotted line). The pQCD fragmentation results are shown with energy losses (shaded band, see the text) and without (dashed line). The STAR data [7] is plotted with the given total errors, and the PHENIX data [9] by adding the given statistical and systematic errors in quadrature. Note the different centrality classes of the two data sets.

Results in Figs. 8 and 9 show that the normalization of the calculated hydrodynamical distributions is essentially independent of the decoupling temperature and because the slopes deviate only at larger transverse momenta, the total charged-particle multiplicity is not very sensitive to the decoupling temperature [3].

If the system continues to undergo hydrodynamical evolution at temperatures below 150 MeV, the collective flow will increase and this is seen as an enhancement of high p_T particles. For $\sqrt{S_{NN}} = 200$ GeV, Fig. 9, the calculation with $T_{\mathrm{dec}} = 120$ MeV overshoots the experimental data already at $p_T \sim 1$ GeV, whereas a high decoupling temperature

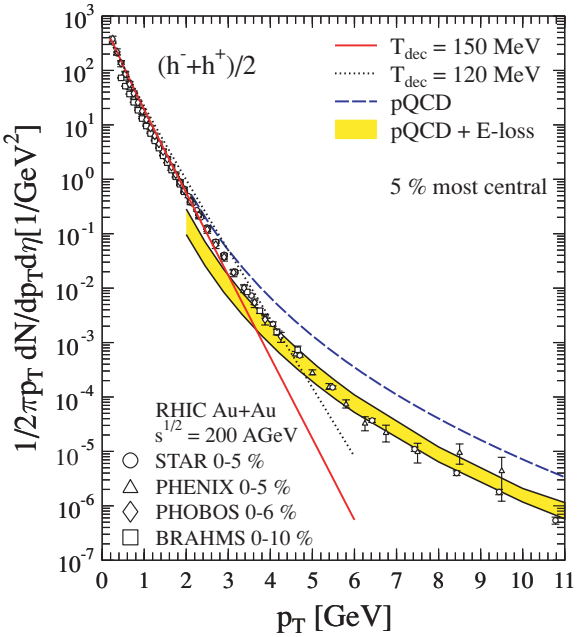

FIG. 9. (Color online) As Fig. 8 but for 5% most central Au+Au collisions at $\sqrt{s_{NN}} = 200$ GeV. The data shown is taken by STAR [6], PHENIX [8], PHOBOS [10], and BRAHMS [11] in the centrality classes indicated. We have plotted the STAR and PHOBOS data with the given total error bars, the PHENIX data by adding the given statistical and systematic errors in quadrature and the BRAHMS data with the given statistical error bars.

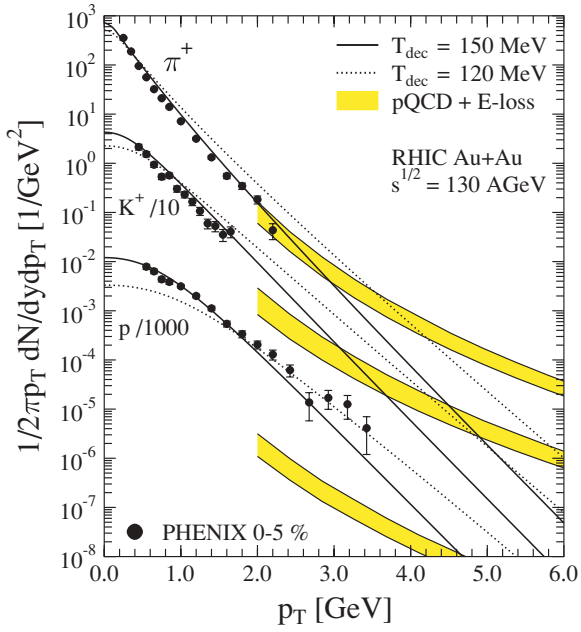

FIG. 10. (Color online) Transverse-momentum spectra of positive pions, positive kaons, and protons at $y = 0$ in 5% most central Au+Au collisions at $\sqrt{s_{NN}} = 130$ GeV. The solid lines show our hydrodynamic results with $T_{\rm dec} = 150$ MeV and the dotted lines the results with $T_{\rm dec} = 120$ MeV. The shaded bands correspond to the pQCD fragmentation results with energy losses. The PHENIX data [103] is plotted with the given total error bars. Note the scaling factors 10 and 1000 for kaons and protons, respectively. Both the hydrodynamic result and the PHENIX data contain the feed-down contributions from hyperons.

$T_{\rm dec} = 150$ MeV describes the results better. It is also clearly seen that the hydrodynamic spectra cannot describe the RHIC data at larger transverse momenta, $p_T \gtrsim 2 \ldots 3$ GeV. The same applicability region for the hydrodynamical spectra at RHIC has been suggested also by the analyses of azimuthal anisotropies (see, e.g., Ref. [69]).

Here it should be emphasized that we have not tuned the computation of the initial state [e.g., the possible unknown constant in the saturation criterion in Eq. (1)] to fit the normalization to the data but kept it as in the original predictions [3,17]. Given the robustness and simplicity of the pQCD+saturation model, we obtain surprisingly good description for pion and kaon spectra. As pions dominate the multiplicity, our results for integrated observables, such as total multiplicity and transverse energy, are also close to the experimental results. Spectra of protons and heavier particles, especially at $\sqrt{s_{NN}} = 200$ GeV, show details that are to be addressed in more detail.

The dashed lines in Figs. 8 and 9 present the spectra of charged hadrons [charged pions, kaons, and (anti-)protons included] from fragmentation of partonic jets as predicted by Eq. (22) in the case of no energy losses. It is seen that this prediction is clearly above the data when p_T grows beyond 4–5 GeV. The solid curves bordering the shaded area are the corresponding upper and lower limits of spectra computed with energy losses as explained in Sec. IV B. In all these pQCD based curves, we apply the $\sqrt{s}$-dependent K factor according to fit II in Eq. (26).

As observed earlier [18] and in these figures, the high-p_T spectrum is clearly suppressed relative to the baseline pQCD fragmentation spectrum without energy losses. When the energy losses are taken into account, the pQCD spectra agree with the data. Apart from the K factor, this agreement is obtained by construction at $\sqrt{s_{NN}} = 200$ GeV because the value of the transport coefficient we use here was determined in Ref. [19] by a fit to the data at $p_T \gtrsim 5$ GeV. It is, however, quite interesting to see how the pQCD fragmentation+energy loss spectrum in turn gradually fails to describe the data at $p_T \lesssim 4 \ldots 5$ GeV. Thus, in the intermediate-p_T region, $2 \ldots 3$ GeV $\lesssim p_T \lesssim 4 \ldots 5$ GeV at RHIC neither the hydrodynamic nor pQCD description is sufficient to describe the data alone but *both* are needed. We will return to this interesting crossover region and the independency of the two approaches in Sec. V C.

Next, we proceed to the p_T spectra of identified hadrons at midrapidities. Figure 10 shows the PHENIX data collected for positive pions, kaons, and protons in 5% most central Au+Au collisions for $y = 0$ at $\sqrt{s_{NN}} = 130$ GeV [103]. Similarly, in Fig. 11 STAR [101], PHENIX [105], and BRAHMS [108,109] data are shown at $\sqrt{s_{NN}} = 200$ GeV. Notice the scaling factors 10 and 1000 for kaons and protons, respectively. The hydrodynamic spectra are computed with a *common* decoupling temperature, i.e., the thermal and the kinetic freeze-out take place simultaneously. The results with a high

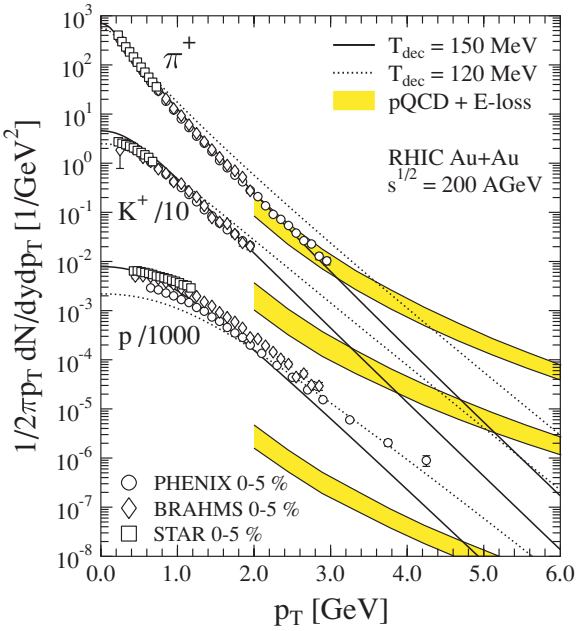

FIG. 11. (Color online) As Fig. 10 but at $\sqrt{s_{NN}} = 200$ GeV. The PHENIX data [105] and the BRAHMS data [108,109] are shown with statistical errors and the STAR data [101] by the given total error bars. The hydrodynamic calculation and the PHENIX data are without the hyperon feed-down contributions but the STAR and BRAHMS data contain the feed-down.

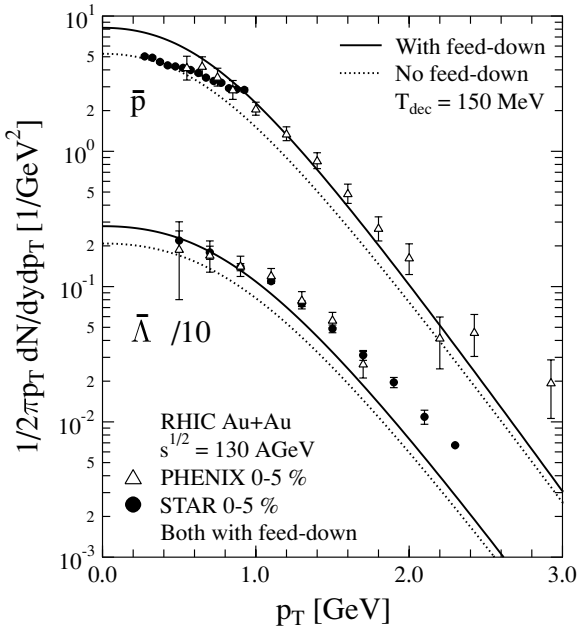

FIG. 12. Transverse-momentum spectra of antiprotons and antilambdas at $y = 0$ in 5% most central Au+Au collisions at $\sqrt{s_{NN}} = 130$ GeV. Our hydrodynamic results are for $T_{dec} = 150$ MeV, the solid lines showing them with hyperon feed-down contributions and the dotted lines without. The PHENIX $\bar{p}$ [103] and $\bar{\Lambda}$ [104] data and the STAR data [102] contain the feed-down contributions. In the PHENIX $\bar{p}$ data the error bars shown correspond to the given total errors, all others to the statistical errors.

decoupling temperature, $T_{dec} = 150$ MeV, are shown by the solid curves, and those with a lower value, $T_{dec} = 120$ MeV, by the dashed ones. It is seen that there is a substantial change in the normalization at small p_T for protons and kaons, indicating also a change in their multiplicity dN/dy. For pions the change in the multiplicity with T_{dec} is small but the slopes change considerably for all three particles. Using a common high decoupling temperature $T_{dec} = 150$ MeV (solid lines) our results describe both the normalization and the slopes of the experimental spectra quite well, whereas for $T_{dec} = 120$ MeV (dotted lines) the normalization of protons and kaons is too low and the p_T dependence of all spectra is too shallow.

The shaded bands in Figs. 10 and 11 show the spectra of pions, kaons (divided by 10), and protons (divided by 1000) calculated from pQCD+ fragmentation+energy loss. For the pion spectra the hydrodynamic and the pQCD calculations complement nicely each other: The former describes the data at low and the latter at high p_T's. Even though tempting, it would be too naive to simply add the two contributions without further considerations. For example, one would expect the thermalization assumption to fail in the large momentum tails of the thermal distribution modifying the region where the dominance of thermal part goes over to the dominance of the pQCD part. See the discussion in Sec. V C. However, for protons at $p_T \sim 3$ GeV, the pQCD fragmentation contribution is clearly smaller than the hydrodynamic one and also clearly below the measured proton spectra. We thus conclude that pQCD fragmentation contribution as considered here is not the origin of the intermediate-p_T proton abundance.

The PHENIX data [103] in Fig. 10 include the feed-down from weak decays of hyperons.[5] Our hydrodynamic spectra are here shown with the feed-down as well. Although for pions and kaons the hyperon feed-down is a small effect, for protons it corresponds to a ∼30% increase. The hyperon feed-down is removed from the $\sqrt{s_{NN}} = 200$ GeV PHENIX data [105] in Fig. 11, but the STAR [101] and BRAHMS [108,109] data include feed-down contributions. Our hydrodynamic results are shown without feed-down.

Our hydrodynamic antiproton and antilambda spectra without (dashed line) and with (solid line) the hyperon feed-down contributions are shown in Fig. 12 for 5% most central Au+Au collisions at $\sqrt{s_{NN}} = 130$ GeV. The data in this figure are from STAR [102] (circles) and PHENIX [104] (triangles) in the corresponding centrality bin. Both data sets include the hyperon feed-down contributions and should thus be reproduced by the solid lines. Again, the agreement is surprisingly good, except at the largest p_T bins.

Because neutral pions produce the most important background for direct and thermal photons [73,110,111], an accurate description of neutral pion spectra would be particularly important. In Fig. 13 we compare our π^0 spectrum with that measured by PHENIX [106] in 10% most central Au+Au collisions at $\sqrt{s_{NN}} = 200$ GeV. Again, the hydrodynamic computation is shown for the low (dotted) and high (solid)

[5]PHENIX has published a feed-down corrected spectrum of antiprotons in minimum bias events [104].

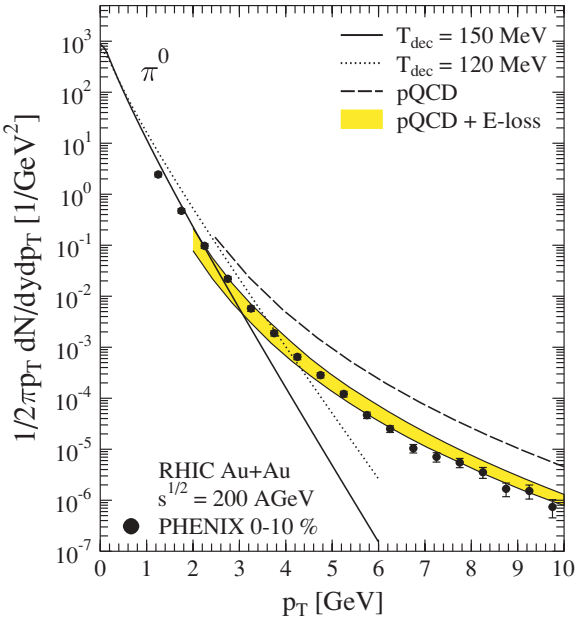

FIG. 13. (Color online) Neutral pion production in 10% most central Au+Au collisions at $\sqrt{s_{NN}} = 200$ GeV. Our hydrodynamic results are shown for $T_{dec} = 150$ MeV (solid line) and $T_{dec} = 120$ MeV (dotted line). The pQCD fragmentation results are shown with energy losses (shaded band, see the text) and without (dashed line). The data is taken by PHENIX [106] and shown with the given total error bars.

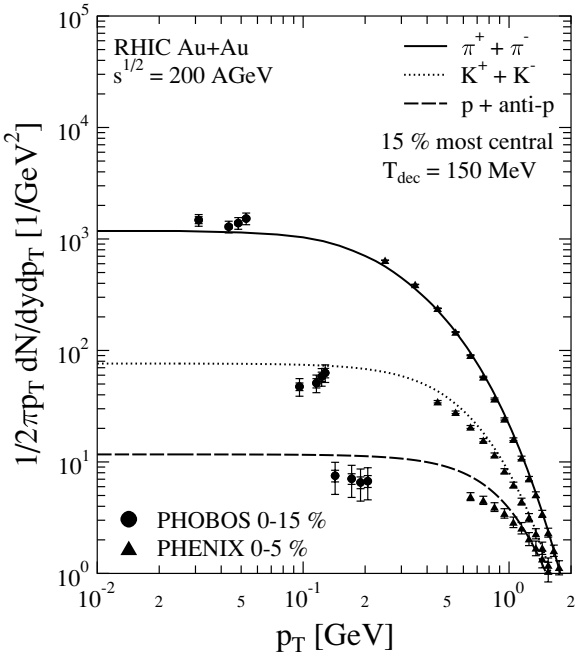

FIG. 14. Transverse momentum spectra of charged pions (solid), charged kaons (dotted), and protons+antiprotons (dashed) at $y = 0$ in 15% most central Au+Au collisions at $\sqrt{s_{NN}} = 200$ GeV in the ultralow-p_T region measured by PHOBOS [107]. Our hydrodynamic results are for $T_{dec} = 150$ MeV. The PHOBOS data is shown with statistical and systematic error bars and the PHENIX data [105] by adding the statistical errors in quadrature. Note the different centrality classes in the two data sets.

T_{dec}, and the pQCD fragmentation+energy loss results, where we assume $\pi^0 = (\pi^+ + \pi^-)/2$ and the K factor from the charged-particle $p + \bar{p}(p)$ data (Fig. 7), are shown by the shaded band. The conclusions here are the same as for charged pions: the high T_{dec} describes the small-p_T part well until $p_T \sim 3$ GeV, whereas the pQCD+energy loss spectrum reproduces the high-p_T part $p_T \gtrsim 5$ GeV. In the intermediate p_T region, $3 \lesssim p_T \lesssim 5$ GeV, both contributions are needed.

Figure 14 shows experimental results for very low transverse-momentum spectra of hadrons measured by the PHOBOS Collaboration [107].

Also the spectra measured by the PHENIX Collaboration [105] extending to larger p_T are shown. Both Collaborations have removed feed-down contributions from their data. Our results for $\pi^+ + \pi^-$, $K^+ + K^-$, and $p + \bar{p}$ are plotted as solid, dotted, and dashed lines, respectively. The measured spectra are quite well reproduced. On a log-scale the small-p_T interval illuminates clearly that also spectrum of pions becomes flat when $p_T < m_\pi$, which is also supported by the PHOBOS data. The spectra of kaons and protons we obtain, are slightly above the data. This is shown in the multiplicities of these particles discussed in the next section.

2. *Multiplicities and feed-down effects*

Experimental results for multiplicities, dN/dy, of $\pi^\pm$, $K^\pm$, p and $\bar{p}$ from PHENIX [105] and STAR [101] Collaborations with $\sqrt{s_{NN}} = 200$ GeV are presented in Table II. PHENIX has subtracted the feed-down from their data, but STAR data include it. Pion and kaon multiplicities in these experiments agree within the given errors. The difference between the PHENIX and STAR results for (anti-)protons, however, may require a more detailed study of the feed-down effects.

Table III summarizes our hydrodynamic results for integrated observables in 5% most central Au+Au collisions at RHIC energies $\sqrt{s_{NN}} = 130$ and 200 GeV. The results are quoted for the decoupling temperatures $T_{dec} = 120$ and 150 MeV. The total and charged particle multiplicities and the total transverse energies at central rapidity are listed first. Below these, we show the total multiplicities for different hadron species. The last three rows of the table show our results for the antibaryon-to-baryon ratios for protons and lambdas and the total net-baryon number.

The first numbers correspond to results in which the hyperon feed-down contributions have not been considered, i.e., we include all the electromagnetic and strong decays but regard those hadrons stable that have only weak decay channels. In the results given in parentheses the hyperon feed-down contributions have been added. The feed-down from Λ, in particular, has been included to all the other yields, whereas the feed-down for Λ comes from the weak decays of Σ, Ξ, and Ω. (Note that Σ^0 decays electromagnetically.)

As seen in Table III, the hyperon feed-down contributions remain small for pions and kaons[6] but are quite significant for

[6]Kaon yields are not affected by the Λ decays.

TABLE II. Experimental results for dN/dy in 5% most central Au+Au collisions with $\sqrt{s_{NN}} = 200$ GeV from PHENIX [105] and STAR [101] Collaborations. The PHENIX results are corrected for the feed-down, in the STAR results feed-down is in the data.

dN/dy	π^+	π^-	K^+	K^-	p	$\bar{p}$
PHENIX	286.4 ± 24.2	281.8 ± 22.8	48.9 ± 6.3	45.7 ± 5.2	18.4 ± 2.6	13.5 ± 1.8
STAR	322 ± 32	327 ± 33	51.3 ± 7.7	49.5 ± 7.4	34.7 ± 6.2	26.7 ± 4.0

lambdas and especially for protons. The number of thermal excitations of heavier hadrons grows with increasing $T_{\rm dec}$ and some of the decay chains of these heavy hadrons end to proton or lambda increasing their yields strongly. Table III shows that, e.g., the number of $\bar{\Lambda}$s goes up by a factor of 4 when $T_{\rm dec}$ is raised from 120 to 150 MeV. A further ∼30–40% increase to p and Λ yields comes from the hyperon feed-down, whereas the ratios $\bar{p}/p$ and $\bar{\Lambda}/\Lambda$ remain almost constant.

Our pion multiplicities in Table III, computed with $T_{\rm dec} = 150$ MeV, agree with both STAR and PHENIX results in Table II. For this $T_{\rm dec}$ we get, however, a slight excess of kaons over the STAR and PHENIX data, as can be seen also in Fig. 11. For protons, our results with feed-down are consistent with the STAR data but the corresponding results without feed-down overshoot the PHENIX data. Table III shows clearly how sensitive the baryon multiplicities are to the decoupling temperature, emphasizing the necessity for a high $T_{\rm dec}$ here.

The baryon multiplicities have also a slight dependence on the number of hadron resonance states included in the EOS. It is, however, not clear how many resonance states should be taken into account. It depends, e.g., on the nature and dynamics of the phase transition and on the lifetime of the hadron gas. There is no guarantee that the number ratios of hadrons at hadronization are the thermal ones. Because the (anti-)quark and gluon structure of hadrons varies, formation of some states could be favored over others. In the hadron gas, interactions among hadrons would drive the densities towards the thermal ones. Because the lifetime of hadron gas is not very long, and the temperature drops fast, especially the formation of heavier states might not be very effective.

Even though the baryon multiplicities are very sensitive to $T_{\rm dec}$, the net-baryon number remains independent of $T_{\rm dec}$, because we have incorporated the conservation of net-baryon current in the hydrodynamic equations [Eq. (14)]. The final net-baryon number thus equals the initial one shown in Table III. Moreover, the net-proton number is almost independent of $T_{\rm dec}$; the change is only a few percentages when $T_{\rm dec}$ changes from 150 to 120 MeV. Thus, the measured net-proton number gives a further probe for the computed initial state,

TABLE III. Multiplicities and total transverse energies without and with feed-down contributions for 5% most central Au+Au collision with $\sqrt{s_{NN}} = 130$ and 200 GeV. Results with feed-down are presented in parentheses. For details, see the text. Also the net-baryon number obtained from Eq. (8) is shown.

$\sqrt{s_{NN}}$ [GeV]	130		200	
$T_{\rm dec}$ [MeV]	120	150	120	150
dN/dy(tot)	1086 (1097)	1141 (1178)	1284 (1297)	1352 (1396)
$dN/d\eta$(tot)	960 (969)	961 (988)	1141 (1152)	1148 (1181)
dN/dy(char)	671 (680)	687 (716)	794 (804)	815 (849)
$dN/d\eta$(char)	597 (604)	587 (608)	710 (718)	701 (726)
dE_T/dy(tot) [GeV]	696 (696)	709 (709)	850 (850)	868 (868)
$dE_T/d\eta$(tot) [GeV]	625 (625)	590 (592)	769 (769)	731 (733)
dN^{π^+}/dy	284 (287)	269 (279)	337 (340)	319 (332)
dN^{π^0}/dy	312 (316)	298 (312)	370 (375)	354 (370)
dN^{π^-}/dy	284 (289)	269 (282)	337 (342)	319 (334)
$dN^{\rm K^+}/dy$	43.6 (43.7)	53.0 (53.1)	51.3 (51.3)	62.4 (62.5)
$dN^{\rm K^-}/dy$	41.1 (41.1)	50.3 (50.4)	49.1 (49.1)	60.1 (60.2)
dN^{p}/dy	10.1 (14.0)	20.5 (30.2)	10.4 (14.5)	23.0 (34.0)
$dN^{\bar{p}}/dy$	3.7 (5.2)	14.0 (21.1)	5.0 (7.1)	17.5 (26.4)
dN^{Λ}/dy	4.1 (5.1)	9.9 (12.9)	4.3 (5.4)	11.2 (14.6)
$dN^{\bar{\Lambda}}/dy$	1.6 (2.0)	7.2 (9.5)	2.1 (2.7)	9.0 (11.8)
$\bar{p}/p$	0.36 (0.37)	0.68 (0.70)	0.48 (0.50)	0.76 (0.78)
$\bar{\Lambda}/\Lambda$	0.39 (0.39)	0.73 (0.74)	0.49 (0.51)	0.80 (0.81)
$dN_{B-\bar{B}}/dy$	16.6		14.0	

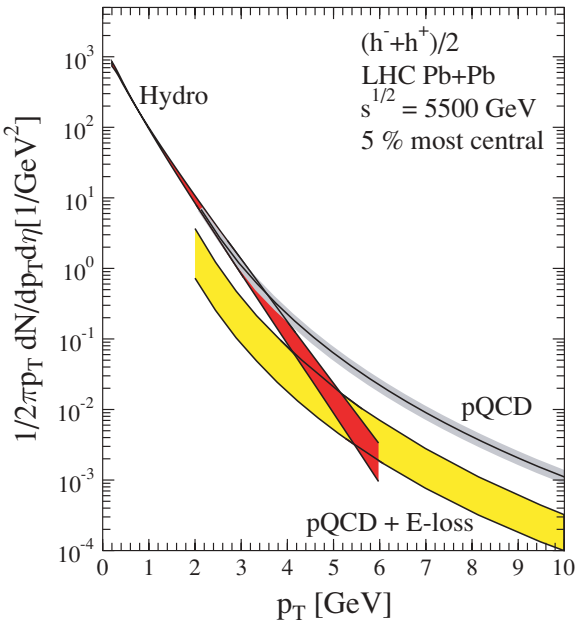

FIG. 15. (Color online) Our prediction for the transverse momentum spectra of charged hadrons at $\eta = 0$ in 5% most central Pb+Pb collisions at the LHC energy $\sqrt{s_{NN}} = 5500$ GeV. The shaded band in the hydrodynamic results shows the sensitivity of our results to $T_{\rm dec}$ in the interval 150 . . . 120 MeV. The solid curve labeled pQCD corresponds to the pQCD fragmentation results where no energy losses have been taken into account. The shaded band related to this is the estimated uncertainty in the extrapolation of the K factor to the LHC energy. The shaded band labeled pQCD+E-loss describes the uncertainty in the pQCD fragmentation results with energy losses (see text for details).

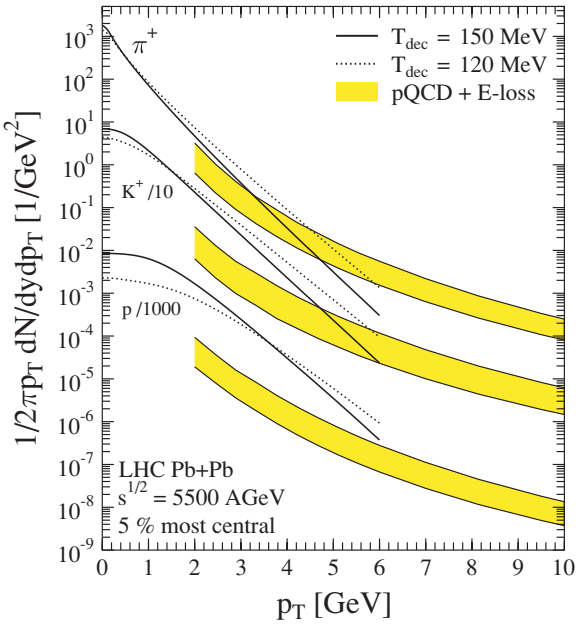

FIG. 16. (Color online) Transverse-momentum spectra predicted for positive pions, positive kaons, and protons at $y = 0$ in 5% most central Pb+Pb collisions at $\sqrt{s_{NN}} = 5500$ GeV. The solid lines show our hydrodynamic results with $T_{\rm dec} = 150$ MeV and the dotted lines the results with $T_{\rm dec} = 120$ MeV. The shaded bands correspond to the pQCD fragmentation results with energy losses.

governed by the saturation scale in our framework. As seen in Tables II and III, our results for the net-proton number agree with the STAR and PHENIX data very well.

B. From RHIC to LHC: spectra and integrated observables

The benefit of a closed calculation for the initial state is that we can predict the hadron spectra, multiplicities, and transverse energies in central $A+A$ collisions also at the LHC. The initial conditions are given in Table I. Without a dynamical model for decoupling (see, e.g., Refs. [112,113]), however, we cannot predict the value for the decoupling temperature. Based on the RHIC results, we would expect $T_{\rm dec}$ to be in the 150 MeV range. To show the sensitivity of our LHC results to $T_{\rm dec}$, we quote them with $T_{\rm dec} = 120$ MeV also.

In Fig. 15 we show the charged particle spectra in 5% most central Pb+Pb collisions at $\sqrt{s_{NN}} = 5500$ GeV from our hydrodynamical calculation with $T_{\rm dec} = 150 \ldots 120$ MeV (the shaded band labeled "Hydro"), as well as from the pQCD+fragmentation with and without energy losses. For the pQCD spectra without the energy losses, the shaded uncertainty band around the solid line stands for the difference between $K_1 \approx 0.65$ from fit I and $K_2 \approx 1.03$ from fit II (see Sec. IV A). In the pQCD calculation with the energy losses included, we apply the latter K factor (fit II has a slightly better χ^2 than fit I), and the large uncertainty band corresponds to the difference between the reweighted and nonreweighted results as discussed in the Sec. IV B.

We see that the hydrodynamical spectra are considerably flatter at the LHC than at RHIC. This is because of the stronger flow developed at the LHC. At the same time, the suppression in the pQCD spectra is larger than at RHIC [19]. The net result of these effects is that the thermal part of the spectrum is expected to dominate over the pQCD tail in a p_T region up to $p_T \sim 4$–5 GeV that is almost twice as wide as that at RHIC where the pQCD tails take over already around $p_T \sim 2$–3 GeV. This will provide an opportunity for more stringent tests of the thermal and hydrodynamical behavior of produced matter, including a wider p_T range where the elliptic flow should follow the hydrodynamical behavior.

Figure 16 shows our prediction for the spectra of positive pions, kaons, and protons at the LHC for the same collision parameters as in the previous figure. The hydrodynamical results are again given with the two different decoupling temperatures, $T_{\rm dec} = 150$ MeV (solid) and $T_{\rm dec} = 120$ MeV (dotted). We show the pQCD fragmentation results with energy losses using $K = 1.03$. The LHC results show similar systematics between the hydrodynamic and pQCD fragmentation results as at RHIC (Figs. 10 and 11; see also Ref. [22]); the crossover region moves to larger p_T for more massive particles.

Integrated observables, total multiplicities and transverse energies, and the multiplicities of different hadron species are given in Table IV for three different decoupling temperatures. Even though the slopes of spectra at $p_T \gtrsim 1 \ldots 2$ GeV depend on $T_{\rm dec}$, the total multiplicity and transverse energy are relatively insensitive on $T_{\rm dec}$ [3]. As at RHIC, only a ∼6%

TABLE IV. Multiplicities and total transverse energies without feed-down contributions for 5% most central Pb+Pb collisions at $\sqrt{s_{NN}} = 5500$ GeV. Also the net-baryon number predicted by Eq. (8) is given.

$T_{\rm dec}$ [MeV]	120	150	160
dN/dy(tot)	4460	4730	4840
$dN/d\eta$(tot)	4120	4240	4290
dN/dy(char)	2760	2850	2900
$dN/d\eta$(char)	2560	2570	2600
dE_T/dy(tot) [GeV]	4010	4070	4110
$dE_T/d\eta$(tot) [GeV]	3790	3710	3680
dN^{π^+}/dy	1170	1120	1120
dN^{π^0}/dy	1290	1240	1240
dN^{π^-}/dy	1170	1120	1120
dN^{K^+}/dy	175	214	218
dN^{K^-}/dy	175	214	218
dN^{p}/dy	25.8	70.8	88.1
$dN^{\bar{p}}/dy$	24.6	69.6	86.9
$\bar{p}/p$	0.95	0.98	0.99
$dN_{B-\bar{B}}/dy$		3.11	

change is seen in dN/dy and a few percentages change in dE_T/dy when changing $T_{\rm dec}$ from 150 to 120 MeV. Note that also at the LHC the pion multiplicity remains quite insensitive to the decoupling temperature. For kaons the change in multiplicity is $\sim$20% (see also Fig. 16 at small p_T) but for (anti-)protons a factor of 2.8. For pions and kaons the change in multiplicity is negligible if $T_{\rm dec}$ is raised from 150 to 160 MeV, whereas the (anti-)proton multiplicity increases $\sim$25%.

As seen in Tables I and IV, we predict an almost net-baryon free central rapidity region at the LHC. The net-baryon number at $y = 0$ is predicted to be down by a factor 5 relative to RHIC. Although the proton and antiproton multiplicities are sensitive to $T_{\rm dec}$, also the net-proton multiplicity, $dN^p/dy - dN^{\bar{p}}/dy$, is practically independent of $T_{\rm dec}$ in the range $T_{\rm dec} = 160 \ldots 120$ MeV. Because of the smallness of the net-proton number relative to the (anti-)proton number, also the antiproton-to-proton ratio $\bar{p}/p = 0.98$ for $T_{\rm dec} = 150$ MeV changes only by a few percents when $T_{\rm dec} = 160 \ldots 120$ MeV.

C. How independent are hydrodynamic and pQCD spectra?

Interestingly, as seen in Figs. 9 and 15, there is quite a large difference between the slopes of the hydrodynamic and pQCD spectra. Our results thus suggest that there is a rather narrow p_T interval in which the dominant hadron production mechanism changes from thermal emission at decoupling to independent partonic jets suffering energy losses. It should be emphasized that we have not attempted to construct an additive two-component model, where the sum of the hydrodynamic and pQCD spectra would give the complete spectra, valid over the whole p_T range. First, in a two-component model we should include only the thermalizing partons, the region $p_{\rm sat} \leqslant q_T \leqslant q_{T\rm th}$, in the computation of the hydrodynamic initial state. Correspondingly, only the nonthermalizing partons, the region $q_T \geqslant q_{T\rm th}$, should be included in the pQCD fragmentation production of hadrons. Second, if we consider energy losses of jet-producing partons, we should add the energy losses back to the hydrodynamic system. Because we do not develop such a two-component model here, and because both computations are now initiated with the same partonic cross sections, one should ask to what extent our hydrodynamical and pQCD fragmentation spectra in Figs. 9 and 15 can be regarded mutually independent, i.e., how much double counting there is if one simply adds the two components together. In the regions where one of the mechanisms dominates, this is obviously not an issue but it becomes especially interesting in the crossover regions $3 \lesssim p_T \lesssim 4$ GeV at RHIC and $5 \lesssim p_T \lesssim 6$ GeV at the LHC, where both components are of equal size. We shall argue below that in these crossover regions (and of course at larger values of p_T), the hydrodynamic and pQCD spectra are in fact biased to different q_T regions of originally produced partons and therefore the two contributions now computed are to a good approximation additive without serious double counting.

Consider first the RHIC spectra for 5% most central Au+Au collisions at $\sqrt{s_{NN}} = 200$ GeV shown in Fig. 9. In the pQCD fragmentation calculation without energy losses, hadrons at $p_T \sim 3$ GeV are dominantly produced by partons at $q_T \sim p_T/\langle z\rangle \approx 1.7 p_T \sim 5.1$ GeV, where $\langle z\rangle \approx 0.6$ follows from the slope of the partonic q_T spectrum and the shape of the (gluonic) fragmentation functions [18,114]. When energy losses are accounted for, the dominating partonic momenta (for a fixed p_T) obviously grow further, typically by, say,[7] a few GeV. Therefore the hadrons at $p_T \sim 3$ GeV produced in pQCD fragmentation+energy loss can be argued to be dominantly produced by partons originally at $q_T \sim 7$ GeV. In particular, the small-q_T region $q_T \lesssim 3.5$ does not contribute much. On the other hand, we notice that in the pQCD+saturation computation of the initial transverse energy, 95% of $\sigma\langle E_T\rangle$ (see Table I) comes from the region $p_{\rm sat} \leqslant q_T \leqslant 3.6$ GeV. Were we to exclude the region $q_T \geqslant q_{T\rm th} = 3.6$ GeV from the calculation of the initial conditions, the hydrodynamic spectra in Fig. 9 would thus decrease only by a few percentages. Similarly, exclusion of the region $q_T \leqslant q_{T\rm th} = 3.6$ GeV from the pQCD fragmentation+energy loss calculation should not visibly decrease the obtained pQCD spectra at $p_T \gtrsim 3$ GeV, or even at $p_T \gtrsim 2$ GeV. Thus we argue that to a good approximation the computed hydrodynamic and pQCD fragmentation+energy loss spectra in Fig. 9 at $p_T \gtrsim 2$ GeV, and especially in the crossover region $3 \lesssim p_T \lesssim 4$ GeV, can be added together without significant double counting. Comparison with the RHIC data also supports this conclusion.

At the LHC, in the 5% most central Pb+Pb collisions shown in Fig. 15, hadrons at $p_T \sim 5$ GeV in the pQCD fragmentation originate dominantly from $q_T \sim 8.5$ GeV partons when energy losses are not accounted for. The average energy losses are now larger than at RHIC, because of the denser system formed. Thus, we argue that with the energy losses included, the $p_T = 5$ GeV hadrons mainly come from partons that are originally

[7] Unfortunately, our current numerical energy loss set up does not allow for a more quantitative estimate at $p_T \leqslant q_{T0}$.

produced at, say, $q_T \sim 11 \ldots 12$ GeV. In particular, the region $q_T \lesssim 6$ GeV should not contribute much to the production of 5 GeV hadrons in the pQCD fragmentation+energy loss computation. On the other hand, for the LHC we notice that 90% of the initial $\sigma \langle E_T \rangle$ comes from $p_{\rm sat} \leqslant q_T \leqslant 6.6$ GeV and, correspondingly, that exclusion of the region $q_T \gtrsim 6.6$ GeV from the initial state computation would reduce the hydrodynamic spectra in Fig. 15 by less than 10%. Thus, again in the crossover region $5 \lesssim p_T \lesssim 6$ GeV and at higher p_T at the LHC, the hydrodynamic and pQCD fragmentation+energy loss spectra can be to a good approximation regarded mutually independent, and the two components in Fig. 15 can be added together.

The basic assumption in the above discussion is that primary small-q_T partons ($q_T \leqslant q_{T\rm th}$) thermalize and the large-q_T partons ($q_T \geqslant q_{T\rm th}$) go through the thermalized matter just suffering energy loss but fragmenting independently. We have argued above that if we set $q_{T\rm th} \sim 3.5$ GeV at RHIC and $q_{T\rm th} \sim 6$ GeV at the LHC, the hydrodynamic and pQCD spectra do not significantly change (reduce) from those shown in Figs. 9 and 15. It should be stressed, however, that the transition from thermalized to jet-producing partons does not take place at any well-defined $q_{T\rm th}$ but is gradual. There are partons in the region around $q_{T\rm th}$ that are not fully thermalized but are not well described by energy-losing independent high-energy partonic jets either. Figure 9 suggests that our hydrodynamic and jet fragmentation components are, when added together, not quite enough to fully explain the RHIC data in the crossover region. This leaves room for an extra contribution from the nonthermalized partons near $q_{T\rm th}$ (e.g., hadronization, recombination [115,116], with the thermal ones) that the present treatment is not sensitive to.

What makes the final shape of the full hadron spectrum in the crossover region very interesting is its dependence on the details of thermalization. A precise experimental determination of the shape provides an extra test for the understanding of thermalization of primary partons.

VI. DISCUSSION

To summarize, we have computed the transverse-momentum spectra of hadrons in central and nearly central $A+A$ collisions at the RHIC and LHC in a broad p_T range. For the low-p_T spectra we apply the hydrodynamic framework with pQCD+saturation initial conditions [3,17]. From the calculated primary production, supplemented with the assumption of adiabatic expansion, we correctly predicted the multiplicities at RHIC [3,17,53]. For the high-p_T part, we make a separate calculation folding together the nuclear PDFs, partonic pQCD cross sections, energy losses, and vacuum fragmentation functions.

Assuming thermalization at formation and no initial transverse flow, we have a closed framework for computing the initial state for radially expanding boost invariant hydrodynamics. Our results show that the main features of the RHIC data on pion, kaon, (anti-)proton, and (anti-)lambda spectra, measured in (nearly) central Au+Au collisions at $p_T \lesssim 2 \ldots 3$ GeV, are quite well reproduced with a single high decoupling temperature $T_{\rm dec} \simeq 150$ MeV. The role of high $T_{\rm dec}$ for simultaneous chemical and kinetic freeze-out is discussed. Also the feed-down contributions from hyperons are studied in detail. We emphasize that the net-baryon multiplicity is predicted by our calculation and our prediction compares fairly well with the RHIC data. Unlike baryon or antibaryon multiplicities, it does not depend on $T_{\rm dec}$, because the net-baryon number is conserved in the hydrodynamical evolution.

The great benefit of a closed framework is that it can be easily extended to the LHC energy. We have presented detailed predictions for hadron spectra in (nearly) central Pb+Pb collisions at LHC that depend both on the calculated initial conditions and the hydrodynamic expansion. The overall multiplicity is less dependent than the spectra on the details of expansion phase and the predicted net-baryon number as a conserved quantity is completely fixed by the calculation of primary production.

The overall behavior of our hydrodynamic results at RHIC looks somewhat different from that at SPS energies. The experimental results for Pb+Pb collisions at SPS are reproduced with a decoupling temperature of the order $T_{\rm dec} \sim 120 \ldots 140$ MeV [24], the lower values somewhat favored by the $p - \bar{p}$ spectrum. That there is a difference in the behavior at SPS and RHIC may not be so surprising because the systems start at quite different densities. At RHIC the matter stays in the plasma state longer and as the matter enters the hadron phase it flows faster than at SPS.

One interesting detail, not studied in this work, is how the transverse profile of the initial energy density [62] affects the flow and the determination of $T_{\rm dec}$. As explained in Sec. II B, here we consider a binary collision profile with a fixed $p_{\rm sat}(A, \sqrt{s_{NN}})$ and fixed $\tau_0 = 1/p_{\rm sat}$. In a central $A+A$ collision, the saturation scales can, however, be expected to grow toward the denser region and decrease toward the edges [60]. This would lower the density at center and increase it at the edges. Also, the center of the system should form earlier than the regions around it. This may have an effect on the transverse profile of initial energy density, as the buildup of transverse collective motion can start earlier at center [61]. Furthermore, the form of the initial transverse profile should in fact depend also on the cms energy because of parton production dynamics in local saturation [60]. These studies are left for later work.

It is quite interesting that with one common decoupling temperature, one can so well reproduce the gross features of the low-p_T hadron spectra measured at midrapidity at RHIC. Certain details, in particular the fall of the proton spectrum from hydrodynamic calculation below the data at $p_T \sim 3$ GeV need, however, improvements. As can be estimated in Figs. 10 and 11, lowering of $T_{\rm dec}$ to 140 MeV would improve the proton spectrum but it would somewhat deteriorate the agreement of the pion and kaon spectra with data. This points to the need of separate chemical and kinetic decoupling in describing the details of all spectra simultaneously. Studies with separate chemical and kinetic decoupling where the stable particle numbers are fixed after chemical freeze-out, show indeed that the spectra of pions and kaons become almost independent of the kinetic decoupling temperature $T_{\rm dec,kin}$, whereas the

(anti-)proton spectra widen with decreasing $T_{\mathrm{dec,kin}}$ [71,74]. As discussed in [71,74], in addition to the hadron spectra, elliptic flow measured as a function of transverse momentum provides a further test on decoupling kinematics. Based on Ref. [71], we would expect that the azimuthal spectra computed with a single high T_{dec} should reasonably well reproduce the elliptic flow measured in noncentral (minimum bias) collisions at midrapidities but that considering chemical decoupling separately from kinetic could yet improve the agreement with the data. A further test is given by the rapidity dependence of elliptic flow. These studies are, however, beyond the scope of the present article. With the azimuthally symmetric boost-invariant setup applied here only rapidity-independent parts of the hadron spectra in central collisions can be considered.

In our collinearly factorized LO pQCD calculation of the high-p_T hadron spectra with absolute normalization, we make use of the K factor's $\sqrt{s}$ systematics demonstrated in Ref. [18]. On top of this baseline calculation, we also add nuclear effects in the PDFs [49] and the energy losses of hard partons in the framework of eikonalized quenching weights [19,20]. The amount of energy losses is controlled by the time(path)-averaged transport coefficient $\hat{q}$. The value of $\hat{q}$ for central Au+Au collisions at $\sqrt{s_{NN}} = 200$ GeV was determined in Ref. [19] by fitting the observed *relative* suppression in the region where hadron-type dependence disappears. The current work, supplementing [19], thus provides an important cross-check of the overall normalization of the computed spectra.

Our pQCD results, extended down to $p_T \sim 2 \ldots 4$ GeV at RHIC, show very interesting relation to the hydrodynamic results. As seen in Figs. 8–11, the pQCD fragmentation+energy loss spectra of charged hadrons and pions merge with the hydrodynamic one quite smoothly in the p_T region where the hydrodynamic calculation starts to fall below the data. As the slopes in these two spectra are quite different, the region of crossing from one mechanism to the other is not sensitive to moderate changes in either contribution. As discussed in Sec. V C, the two results can be to a good approximation considered independent in the crossover region and at higher p_T.

In particular, we can confirm that the difference between the proton data at $p_T \sim 3$ GeV and the hydrodynamic results for $T_{\mathrm{dec}} = 150$ MeV cannot be explained by pQCD fragmentation+energy loss results considered here. As discussed above, a separate chemical and kinetic freeze-out seems to keep the spectra of kaons and pions almost independent of but widens the proton spectrum so that the present data that ends at $p_T \approx 3.7$ GeV can be described with hydro calculation. It would be extremely interesting if the measured p_T range of the proton spectrum could be extended up to 6. . .7 GeV. We would expect the pQCD calculation of jet fragmentation with energy loss to reproduce the data in that region and the possible deficit of predicted spectra, if any, should show up in the p_T interval from 4 to 6 GeV. We also note that both the proton excess and elliptic flow in the intermediate p_T region have been successfully explained in terms of recombining partons, see Refs. [115,116] and references therein. As we have discussed in Sec. V C, in addition to the hydrodynamical and the pQCD fragmentation components, there appears to be room for recombination, especially in the case where one of the recombining partons originates from jet quenching but is not fully thermalized, and the other parton is thermal. Hadrons from such recombination are not accounted for in the present study.

As discussed in detail above, our prediction for the high-p_T spectra at the LHC is subject to uncertainties arising from the extrapolation of the K factor and transport coefficient into a new energy and density regime and from the normalization of the quenching weights. In particular, the uncertainties related to using the quenching weights with finite kinematics are quite large up to $p_T \sim 100$ GeV [19]. The uncertainty of the K factor can be reduced by scale-optimized NLO calculations [88] and by applying the latest NLO nPDFs [117] and, ultimately, by comparison with the hadron spectra to be measured in $p+p$ and $p+A$ collisions at the LHC. Implementation of quenching weights into the NLO pQCD framework will be a challenging task for the future. The most urgent need would obviously be the inclusion of finite kinematics in the computation of the quenching weights. Also the effects of detailed hydrodynamic evolution with transverse expansion of the dense partonic system should be implemented into the energy loss calculation.

ACKNOWLEDGMENTS

We thank P. Huovinen, J. Rak, D. Rischke, C. Salgado, K. Tuominen, and U. Wiedemann for discussions. This work was financially supported by the Academy of Finland, projects 50338 and 206024. H. Honkanen gratefully acknowledges the financial support from the Wihuri foundation.

[1] [STAR Collaboration], Phys. Rev. C **70**, 054907 (2004); S. S. Adler *et al.* (PHENIX Collaboration), dE(T)/d Phys. Rev. C **71**, 034908 (2005) [Erratum-*ibid.* C **71**, 049901 (2005)].

[2] J. D. Bjorken, Phys. Rev. D **27**, 140 (1983).

[3] K. J. Eskola, P. V. Ruuskanen, S. S. Räsänen, and K. Tuominen, Nucl. Phys. **A696**, 715 (2001).

[4] J. Adams *et al.* (STAR Collaboration), Phys. Rev. C **72**, 014904 (2005); S. S. Adler *et al.* (PHENIX Collaboration), Phys. Rev. Lett. **91**, 182301 (2003); B. B. Back *et al.* (PHOBOS Collaboration), arXiv:nucl-ex/0407012.

[5] P. F. Kolb, Proc. Strong and Electroweak Matter 2004, Helsinki, June 2004, edited by K. J. Eskola *et al.*, World Scientific 2005.

[6] J. Adams *et al.* (STAR Collaboration), Phys. Rev. Lett. **91**, 172302 (2003).

[7] C. Adler *et al.* (STAR Collaboration), collisions Phys. Rev. Lett. **89**, 202301 (2002).

[8] S. S. Adler *et al.* (PHENIX Collaboration), Phys. Rev. C **69**, 034910 (2004).

[9] K. Adcox *et al.* (PHENIX Collaboration), Au Phys. Rev. Lett. **88**, 022301 (2002).

[10] B. B. Back *et al*. (PHOBOS Collaboration), at Phys. Lett. **B578**, 297 (2004).

[11] I. Arsene *et al*. (BRAHMS Collaboration), Phys. Rev. Lett. **91**, 072305 (2003).

[12] I. Vitev, J. Phys. G **30**, S791 (2004); K. Filimonov, J. Phys. G **30**, S919 (2004); LHC," U. A. Wiedemann, Proc. of Strong and Electroweak Matter 2004, Helsinki June 2004, edited by K. J. Eskola *et al*., World Scientific 2005; and references therein.

[13] S. S. Adler *et al*. (PHENIX Collaboration), momentum Phys. Rev. Lett. **91**, 072303 (2003); J. Adams *et al*. (STAR Collaboration), p(T) Phys. Rev. Lett. **91**, 072304 (2003).

[14] C. Adler *et al*. (STAR Collaboration), Au+Phys. Rev. Lett. **90**, 082302 (2003).

[15] U. W. Heinz and P. F. Kolb, Nucl. Phys. **A702**, 269 (2002); D. Magestro, J. Phys. G **31**, 265 (2005).

[16] H. Von Gersdorff, L. McLerran, M. Kataja, and P. V. Ruuskanen, In Phys. Rev. D **34**, 794 (1986); **34** 2755, (1986).

[17] K. J. Eskola, K. Kajantie, P. V. Ruuskanen, and K. Tuominen, and Nucl. Phys. **B570**, 379 (2000).

[18] K. J. Eskola and H. Honkanen, hadronic Nucl. Phys. **A713**, 167 (2003).

[19] K. J. Eskola, H. Honkanen, C. A. Salgado, and U. A. Wiedemann, Nucl. Phys. **A747**, 511 (2005).

[20] C. A. Salgado and U. A. Wiedemann, Phys. Rev. D **68**, 014008 (2003).

[21] T. Hirano and Y. Nara, Nucl. Phys. **A743**, 305 (2004); J. Phys. G **30**, S1139 (2004).

[22] T. Hirano and Y. Nara, Phys. Rev. C **69**, 034908 (2004).

[23] P. Huovinen, P. V. Ruuskanen, and J. Sollfrank, Nucl. Phys. **A650**, 227 (1999).

[24] J. Sollfrank, P. Huovinen, M. Kataja, P. V. Ruuskanen, M. Prakash, and R. Venugopalan, Phys. Rev. C **55**, 392 (1997).

[25] J. P. Blaizot and A. H. Mueller, Nucl. Phys. **B289**, 847 (1987).

[26] K. Kajantie, P. V. Landshoff, and J. Lindfors, Phys. Rev. Lett. **59**, 2527 (1987).

[27] K. J. Eskola, K. Kajantie, and J. Lindfors, Nucl. Phys. **B323**, 37 (1989).

[28] X. N. Wang and M. Gyulassy, Phys. Rev. D **44**, 3501 (1991).

[29] L. V. Gribov, E. M. Levin, and M. G. Ryskin, Phys. Rep. **100**, 1 (1983).

[30] V. S. Fadin, E. A. Kuraev, and L. N. Lipatov, Phys. Lett. **B60**, 50 (1975); I. I. Balitsky and L. N. Lipatov, Sov. J. Nucl. Phys. **28**, 822 (1978) [Yad. Fiz. **28**, 1597 (1978)].

[31] Y. L. Dokshitzer, Sov. Phys. JETP **46**, 641 (1977) [Zh. Eksp. Teor. Fiz. **73**, 1216 (1977)]; V. N. Gribov and L. N. Lipatov, Sov. J. Nucl. Phys. **15**, 438, 675 (1972) [Yad. Fiz. **15**, 781, 1218 (1972); P. G. Altarelli and G. Parisi, Nucl. Phys. **B126**, 298 (1977).

[32] A. M. Stasto, K. Golec-Biernat, and J. Kwiecinski, Phys. Rev. Lett. **86**, 596 (2001); K. Golec-Biernat and M. Wusthoff, Phys. Rev. D **60**, 114023 (1999); **59**, 014017 (1999).

[33] A. H. Mueller and J. Qiu, Nucl. Phys. **B268**, 427 (1986).

[34] K. J. Eskola, H. Honkanen, V. J. Kolhinen, J. W. Qiu, and C. A. Salgado, Nucl. Phys. **B660**, 211 (2003).

[35] K. J. Eskola, H. Honkanen, V. J. Kolhinen, J. W. Qiu, and C. A. Salgado, arXiv:hep-ph/0302185.

[36] N. Armesto, Eur. Phys. J. C **26**, 35 (2002).

[37] D. Kharzeev and E. Levin, Phys. Lett. **B523**, 79 (2001).

[38] D. Kharzeev, E. Levin, and M. Nardi, Phys. Rev. C **71**, 054903 (2005); Nucl. Phys. **A747**, 609 (2005).

[39] K. J. Eskola, K. Kajantie, and P. V. Ruuskanen, Eur. Phys. J. C **1**, 627 (1998).

[40] K. Morita, S. Muroya, C. Nonaka, and T. Hirano, Phys. Rev. C **66**, 054904 (2002).

[41] K. J. Eskola, K. Kajantie, P. V. Ruuskanen, and K. Tuominen, Phys. Lett. **B543**, 208 (2002).

[42] L. McLerran and R. Venugopalan, Phys. Rev. D **49**, 2233 (1994); **49**, 3352, (1994); Phys. Rev. D **50**, 2225 (1994).

[43] J. P. Blaizot and F. Gelis, Nucl. Phys. **A750**, 148 (2005); H. Weigert, *Proceedings of Strong and Electroweak Matter 2004*, Helsinki June 2004, edited by K. J. Eskola *et al*. (World Scientific, Singapore, 2005); J. Jalilian-Marian, J. Phys. G **30**, S751 (2004).

[44] A. Krasnitz, Y. Nara, and R. Venugopalan, Phys. Rev. Lett. **87**, 192302 (2001).

[45] K. J. Eskola, Nucl. Phys. **A698**, 78 (2002).

[46] T. Lappi, Phys. Rev. C **67**, 054903 (2003).

[47] A. Freund, K. Rummukainen, H. Weigert, and A. Schafer, Phys. Rev. Lett. **90**, 222002 (2003).

[48] N. Armesto, C. A. Salgado, and U. A. Wiedemann, Phys. Rev. Lett. **94**, 022002 (2005).

[49] K. J. Eskola, V. J. Kolhinen, and C. A. Salgado, Eur. Phys. J. C **9**, 61 (1999); K. J. Eskola, V. J. Kolhinen, and P. V. Ruuskanen, Nucl. Phys. **B535**, 351 (1998).

[50] K. J. Eskola and K. Tuominen, Phys. Lett. **B489**, 329 (2000); Phys. Rev. D **63**, 114006 (2001).

[51] K. J. Eskola and K. Kajantie, Z. Phys. C **75**, 515 (1997).

[52] K. J. Eskola, B. Muller, and X. N. Wang, Phys. Lett. **B374**, 20 (1996).

[53] P. V. Ruuskanen, Nucl. Phys. **A702**, 259 (2002); K. J. Eskola, Nucl. Phys. **A702**, 249 (2002).

[54] K. J. Eskola, H. Niemi, P. V. Ruuskanen, and S. S. Räsänen, Phys. Lett. **B566**, 187 (2003).

[55] K. J. Eskola, H. Niemi, P. V. Ruuskanen, and S. S. Räsänen, Nucl. Phys. **A715**, 561 (2003).

[56] W. Broniowski and W. Florkowski, Phys. Rev. Lett. **87**, 272302 (2001).

[57] S. D. Ellis, Z. Kunszt, and D. E. Soper, Phys. Rev. Lett. **64**, 2121 (1990).

[58] A. Bohr and B. R. Mottelson, *Nuclear Structure I* (Benjamin, New York, 1969).

[59] M. Glück, E. Reya, and A. Vogt, Z. Phys. C **67**, 433 (1995).

[60] K. J. Eskola, K. Kajantie, and K. Tuominen, Phys. Lett. **B497**, 39 (2001).

[61] P. F. Kolb, U. W. Heinz, P. Huovinen, K. J. Eskola, and K. Tuominen, Nucl. Phys. **A696**, 197 (2001).

[62] P. Huovinen, Nucl. Phys. **A715**, 299 (2003).

[63] K. J. Eskola, K. Kajantie, and K. Tuominen, Nucl. Phys. **A700**, 509 (2002).

[64] P. Arnold, J. Lenaghan, and G. D. Moore, JHEP 0308 (2003) 002; P. Arnold, J. Lenaghan, G. D. Moore, and L. G. Yaffe, Phys. Rev. Lett. **94**, 072302 (2005).

[65] A. Rebhan, P. Romatschke, and M. Strickland, Phys. Rev. Lett. **94**, 102303 (2005).

[66] R. Baier, A. H. Mueller, D. Schiff, and D. T. Son, Phys. Lett. **B502**, 51 (2001).

[67] H. Niemi *et al*., in hep-ph/0311131.

[68] I. G. Bearden *et al*. (BRAHMS Collaboration), Phys. Rev. Lett. **88**, 202301 (2002).

[69] P. F. Kolb and U. Heinz, in R. C. Hwa (edited by) *et al*.: *Quark Gluon Plasma 3* (World Scientific, Singapore, 2004), p. 634-714.

[70] T. Hirano, Phys. Rev. C **65**, 011901 (2002).
[71] T. Hirano and K. Tsuda, Phys. Rev. C **66**, 054905 (2002).
[72] T. Hirano and Y. Nara, Phys. Rev. C **66**, 041901 (2002); Phys. Rev. Lett. **91**, 082301 (2003); Phys. Rev. C **68**, 064902 (2003).
[73] P. Huovinen, P. V. Ruuskanen, and S. S. Räsänen, Phys. Lett. **B535**, 109 (2002).
[74] P. F. Kolb and R. Rapp, Phys. Rev. C **67**, 044903 (2003).
[75] K. Rajagopal, Acta Phys. Pol. B **31**, 3021 (2000) [Comments Nucl. Part. Phys. A **2**, 120 (2002 APCPC,549,95-119.2002)].
[76] F. Karsch, J. Phys. G **31**, S633 (2005).
[77] F. Karsch and E. Laermann, arXiv:hep-lat/0305025, R. C. Hwa *et al*. (eds.), Quark-Gluon Plasma III, 1–59 (World Scientific, Singapore, 2004).
[78] G. M. Welke, R. Venugopalan, and M. Prakash, Phys. Lett. **B245**, 137 (1990); R. Venugopalan and M. Prakash, Nucl. Phys. **A546**, 718 (1992).
[79] R. A. Schneider and W. Weise, Phys. Rev. C **64**, 055201 (2001).
[80] P. Huovinen, heavy arXiv:nucl-th/0505036.
[81] P. V. Ruuskanen, Acta Phys. Pol. B **18**, 551 (1987).
[82] F. Cooper and G. Frye, Phys. Rev. D **10**, 186 (1974).
[83] K. Hagiwara *et al*. (Particle Data Group Collaboration), Phys. Rev. D **66**, 010001 (2002).
[84] J. Sollfrank, P. Koch, and U. W. Heinz, Z. Phys. C **52**, 593 (1991).
[85] J. Adams *et al*. (STAR Collaboration), arXiv:nucl-ex/0311017.
[86] E. Schnedermann, J. Sollfrank, and U. Heinz, Phys. Rev. C **48**, 2462 (1993).
[87] F. M. Borzumati and G. Kramer, Z. Phys. C **67**, 137 (1995).
[88] P. Aurenche, M. Fontannaz, J. P. Guillet, B. A. Kniehl, and M. Werlen, Eur. Phys. J. C **13**, 347 (2000).
[89] X. N. Wang, Phys. Rev. C **61**, 064910 (2000).
[90] Y. Zhang, G. Fai, G. Papp, G. G. Barnaföldi, and P. Levai, Phys. Rev. C **65**, 034903 (2002).
[91] I. Vitev, Phys. Lett. **B562**, 36 (2003); arXiv:hep-ph/0212109.
[92] B. A. Kniehl, G. Kramer, and B. Potter, Nucl. Phys. **B582**, 514 (2000).
[93] H. L. Lai *et al*. (CTEQ Collaboration), Eur. Phys. J. C **12**, 375 (2000).
[94] T. Akesson *et al*. (Axial Field Spectrometer Collaboration), Nucl. Phys. **B209**, 309 (1982).
[95] C. Albajar *et al*. (UA1 Collaboration), Phys. At. Nucl. **B335**, 261 (1990).
[96] G. Bocquet *et al*., Phys. Lett. **B366**, 434 (1996).
[97] F. Abe *et al*. (CDF Collaboration), Phys. Rev. Lett. **61**, 1819 (1988).
[98] R. Baier, Nucl. Phys. **A715**, 209 (2003).
[99] C. A. Salgado and U. A. Wiedemann, Phys. Rev. Lett. **89**, 092303 (2002); M. Gyulassy, P. Levai, and I. Vitev, Phys. Lett. **B538**, 282 (2002); X. N. Wang, Z. Huang, and I. Sarcevic, Phys. Rev. Lett. **77**, 231 (1996).
[100] C. A. Salgado and U. A. Wiedemann, Phys. Rev. Lett. **93**, 042301 (2004).
[101] J. Adams *et al*. (STAR Collaboration), Phys. Rev. Lett. **92**, 112301 (2004).
[102] C. Adler *et al*. (STAR Collaboration), Phys. Rev. Lett. **89**, 092301 (2002).
[103] K. Adcox *et al*. (PHENIX Collaboration), Phys. Rev. Lett. **88**, 242301 (2002).
[104] K. Adcox *et al*. (PHENIX Collaboration), Phys. Rev. Lett. **89**, 092302 (2002).
[105] S. S. Adler *et al*. (PHENIX Collaboration), Phys. Rev. C **69**, 034909 (2004).
[106] S. S. Adler *et al*. (PHENIX Collaboration), Phys. Rev. Lett. **91**, 072301 (2003).
[107] B. B. Back *et al*. (PHOBOS Collaboration), arXiv:nucl-ex/0401006.
[108] I. G. Bearden *et al*. (BRAHMS Collaboration), Phys. Rev. Lett. **94**, 162301 (2005).
[109] I. G. Bearden *et al*. (BRAHMS Collaboration), Phys. Rev. Lett. **93**, 102301 (2004).
[110] S. S. Räsänen, Nucl. Phys. **A715**, 717 (2003).
[111] P. Aurenche, H. Delagrange, and P. V. Ruuskanen, in arXiv:hep-ph/0311131.
[112] D. Teaney, J. Lauret, and E. V. Shuryak, Nucl. Phys. **A698**, 479 (2002).
[113] D. Teaney, J. Lauret, and E. V. Shuryak, arXiv:nucl-th/0110037.
[114] R. Vogt, Phys. Rev. C **70**, 064902 (2004).
[115] R. C. Hwa, arXiv:nucl-th/0501054.
[116] C. Nonaka, B. Mueller, S. A. Bass, R. J. Fries, and M. Asakawa, J. Phys. G **31**, S429 (2005).
[117] D. de Florian and R. Sassot, Phys. Rev. D **69**, 074028 (2004).